Fatigue Performance of Exfoliated E-8C Upper Wing Skin Material

Molly R. Brown
Scott A. Fawaz

Center for Aircraft Structural Life Extension
Department of Engineering Mechanics

United States Air Force Academy
Colorado Springs, Colorado 80840

October 2004

APPROVED FOR PUBLIC RELEASE; DISTRIBUTION UNLIMITED

DEAN OF THE FACULTY
UNITED STATES AIR FORCE ACADEMY
COLORADO 80840

USAFA-TR-04-07

This technical report, **Fatigue Performance of Exfoliated E-8C Upper Wing Skin Material**, is presented as a competent treatment of the subject, worthy of publication. The United States Air Force Academy vouches for the quality of the research, without necessarily endorsing the opinions and conclusions of the authors. Therefore, the views expressed in this article are those of the authors and do not reflect the official policy or position of the United States Air Force, Department of Defense, or the US Government.

This report has been cleared for open publication and public release by the appropriate Office of Information in accordance with AFI 61-202 and USAFA FOI 190-1. This report may have unlimited distribution.

Molly R. Brown — 20 October 2004
Research Engineer — Date

SCOTT A. FAWAZ, Lt Col, USAF — 21 October 2004
Director — Date
Center for Aircraft Structural Life Extension

Abstract

The Center for Aircraft Structural Life Extension (CAStLE) at the United States Air Force Academy investigated the fatigue performance in terms of total life of artificially exfoliated E-8C upper wing skin as part of the Aeronautical Systems Center, Agile Combat Support Squadron's (ASC/AAA) Air Vehicles Health Management program. The specimens were hourglass in shape to ensure a uniform stress distribution through the width of the gage section. They were corroded on three material orientations, LT, ST, and LS and subjected to the compression-dominated load spectrum of the E-8C at upper wing station (UWS) 320. The specimens were loaded in both the LT and TL direction. Fatigue testing was done on spanwise (LT) and chordwise (TL) oriented specimens. An electrochemical corrosion process was performed by the Fontana Corrosion Center at the Ohio State University on the 7178-T6 aluminum to create intergranular corrosion (IC) followed by exfoliation corrosion (EC). The first set of fatigue tests, simulating two aircraft design lifetimes, was completed with no failures in the 18 specimens. All specimens were then tested again using a modified load spectrum which increased the spectrum tensile peak stresses by 20%. Eight of eighteen specimens survived the second, more severe, spectrum without failure. After completion of the fatigue tests, the specimens were analyzed using optical and electron microscopy to determine the area and volume of the corroded region in addition to the size and location of the crack nucleation site.

Contents

List of Figures

List of Tables

1. Introduction

The Aeronautical Systems Center, Agile Combat Support Squadron (ASC/AAA) has developed an Air Vehicle Health Management program to address cyclical and time dependent material and structural degradation in the USAF aircraft fleet. The purpose of this report is to document the results of a project conducted by the Center for Aircraft Structural Life Extension (CAStLE), Department of Engineering Mechanics, United States Air Force Academy for ASC/AAA to assess the fatigue performance of artificially corroded E-8C upper wing skin (UWS) material, aluminum alloy 7178-T6.

To assess the structural integrity in a fatigue context of corroded upper wing skin material, spectrum loading fatigue tests were conducted of laboratory exfoliated specimens on actual aircraft material. The specimens were machined by S&K Technologies, corroded by the Fontana Corrosion Center at the Ohio State University, and fatigue tested and analyzed at the United States Air Force Academy by CAStLE.

In order to consider extending the service life and possibly deferring maintenance, the fatigue criticality of the exfoliated specimens must be determined. In other words, will mode I fatigue cracks nucleate in the corroded upper wing skin? Figure 1 illustrates the three modes of crack surface displacement.

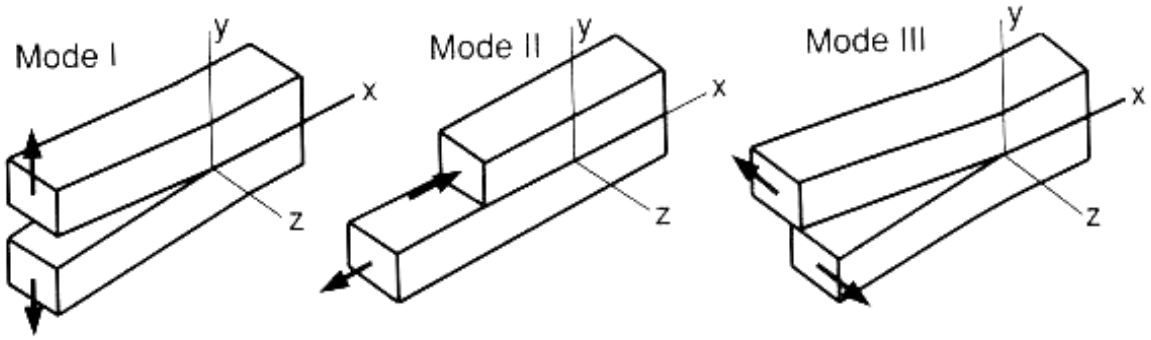

Figure 1. The three modes of crack surface displacement, from Dowling (1). Mode I: opening; Mode II: sliding; Mode III: tearing.

Deferring maintenance of exfoliation corrosion will reduce the USAF's yearly cost of corrosion; however, safety is paramount. The most common method of repair for EC is mechanically removing the damaged material with a grinding disk, pad, or wheel. This method is commonly referred to as grind-out or blend-out. To defer maintenance, the maintainer will need to know if the EC will nucleate a crack. In this effort, the effects of deferring maintenance is investigated via evaluation of crack nucleation in three corrosion orientations and two loading directions.

2. Background

Exfoliation corrosion occurs on the UWS due to protective coating breakdown between the cadmium plated steel fasteners and the aluminum alloy 7178-T6. Once the protective cadmium coating is ineffective, a galvanic cell is created between the steel fasteners and the UWS. The galvanic scale (see Table 1) is chemically representative of a material's potential for activity as a corrosive compound. Galvanic corrosion can occur when two dissimilar metals (from differing electromotive groups) or alloys are joined in the presence of an electrolyte. The farther apart they lie on the chart, corrosion will happen much more quickly. In a galvanic cell, the anode loses material which is deposited on the cathode. Materials in the lower numbered groups are more anodic and in the higher numbered groups more cathodic. For the E-8C, the aluminum UWS is suffering the volumetric loss.

Table 1. Galvanic corrosion susceptibility increases as materials from different electromotive groups are chosen to contact, from Niu (2).

Electromotive Group	Metal or Alloy
Group I	All magnesium alloys
Group II	All aluminum alloys, zinc, cadmium, and nickel-zinc alloy
Group III	Steel, cast iron, lead, tin, lead-tin solder, and 400 series stainless steel
Group IV	200, 300, and 400 series stainless steel, precipitation hardening steel (PH 13-8Mo 15-5 PH, 17-4 PH, 17-7 PH, AM 350, A-286), nickel, inconel, monel, titanium, chronium, silver, copper, brass, bronze, 70 Cu-30 Ni and Halestoy B
Group V	Graphite, gold, and platinum

Figure 2 shows severe exfoliation corrosion at multiple sites around rivet holes.

Figure 2. Exfoliation corrosion at multiple sites, each near rivet holes.

Schematically shown in Figure 3, the intergranular corrosion fissures, due to galvanic corrosion, can occur at locations around the fastener hole where fatigue cracks are commonly expected to nucleate. In turn, this creates intergranular corrosion at sites along the rivet hole. Severe attack may result in entire grains being dislodged from the base material from extreme separation at the grain boundaries. Exfoliation is the result. The goal of this effort is to determine if fatigue cracks will nucleate from IC and EC damage when the applied load spectrum is compression dominant, as experienced in the upper wing skin.

Figure 3. Intergranular corrosion is often found to start near rivet holes. This type of microstructure is commonly found in 7XXX alloys.

3. Experimental Investigation

The hourglass specimens were machined from actual UWS aircraft material—AA 7178. Since exfoliation corrosion is found in a variety of conditions, loading directions for the test were chosen to be both longitudinal and transverse. For a diagram showing where the material originated, see Figure 4 and Figure 5.

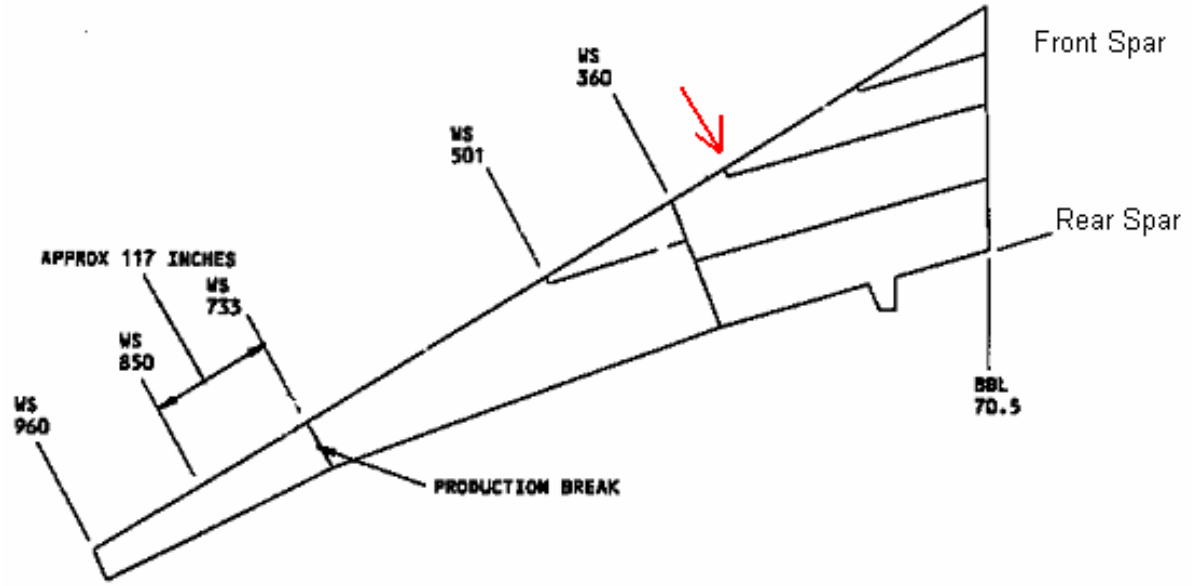

Figure 4. Wing station layout with arrow pointing to area of interest.

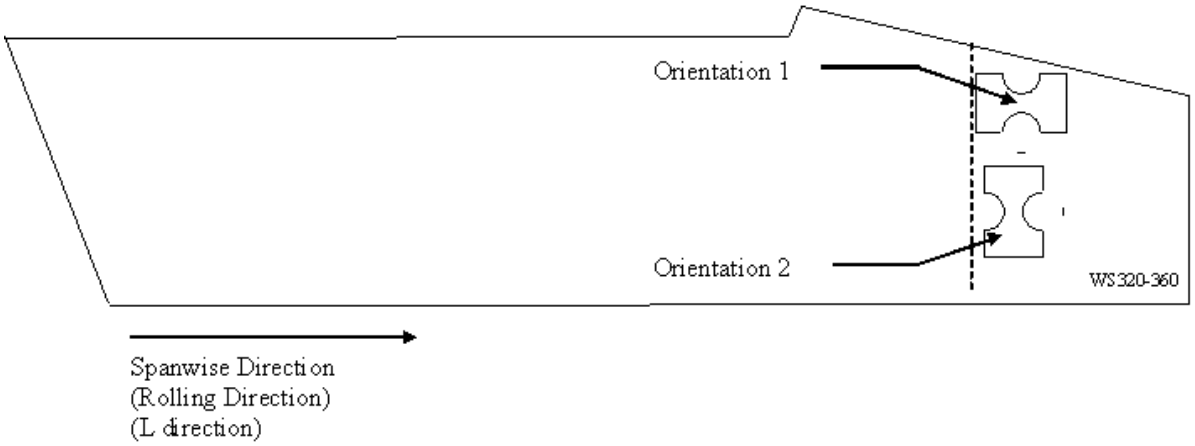

Figure 5. Wing section 320 through 360 on the upper wing skin with specimen cut-out locations shown.

Face milling was completed which ensured proper specimen thickness. The specimens were then machined to size as in Figure 6 and Figure 7.

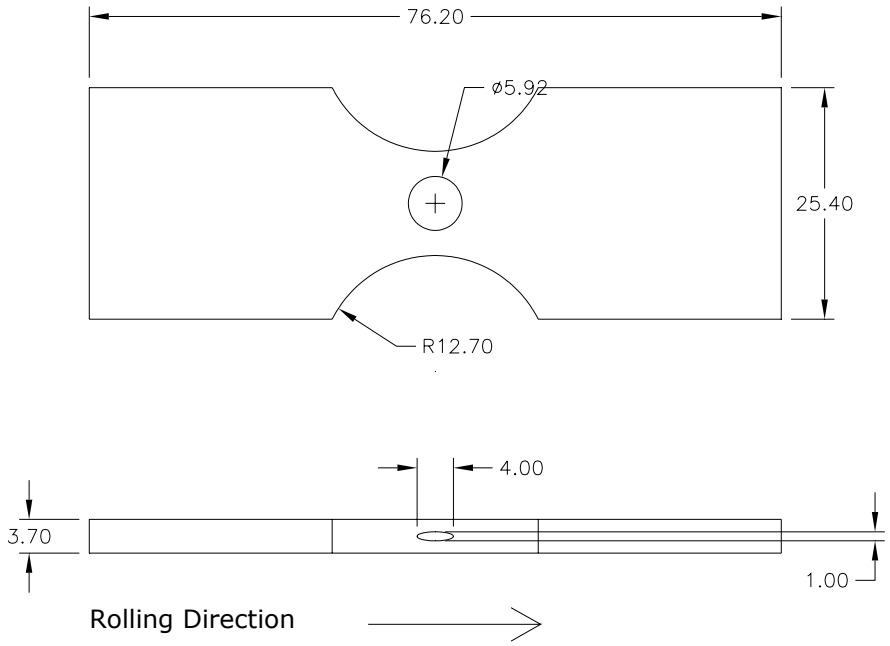

Figure 6. One of the specimen configurations with the loading and longitudinal directions the same. Corrosion occurs on both the LT and LS planes, shown with the dimensioned circle and ellipse. Dimensions are in mm.

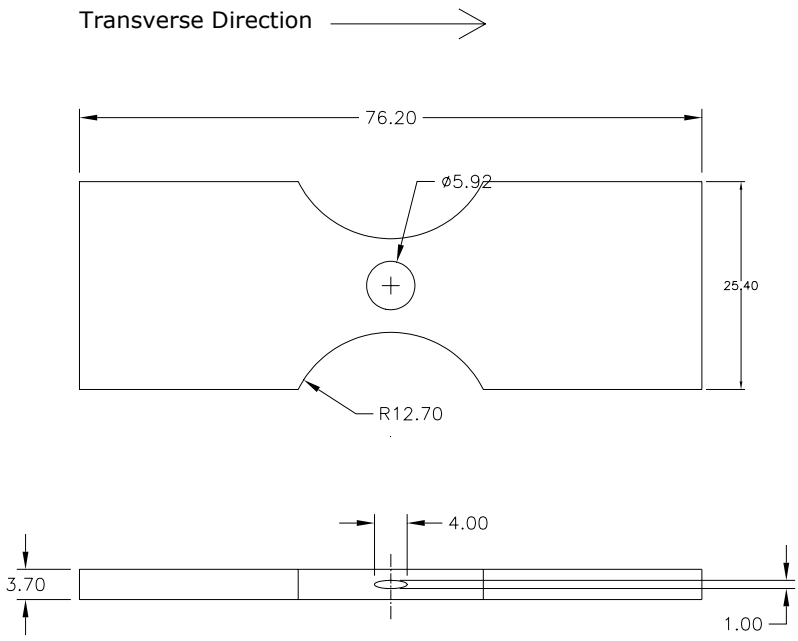

Figure 7. One of the specimen configurations with the loading and transverse directions the same. Corrosion occurs on both the LT and LS planes, shown with the dimensioned circle and ellipse in mm.

A dimple was milled slightly into the surface to simulate corrosion through the S direction of the material, which has been found to be the most corrosion resistant direction microstructurally. Foil penetration tests were done at the Fontana Corrosion Center to

measure growth kinetics (see Figure 8). The test measures time for the fastest-growing localized corrosion site to penetrate through the foil, which provides growth kinetics.

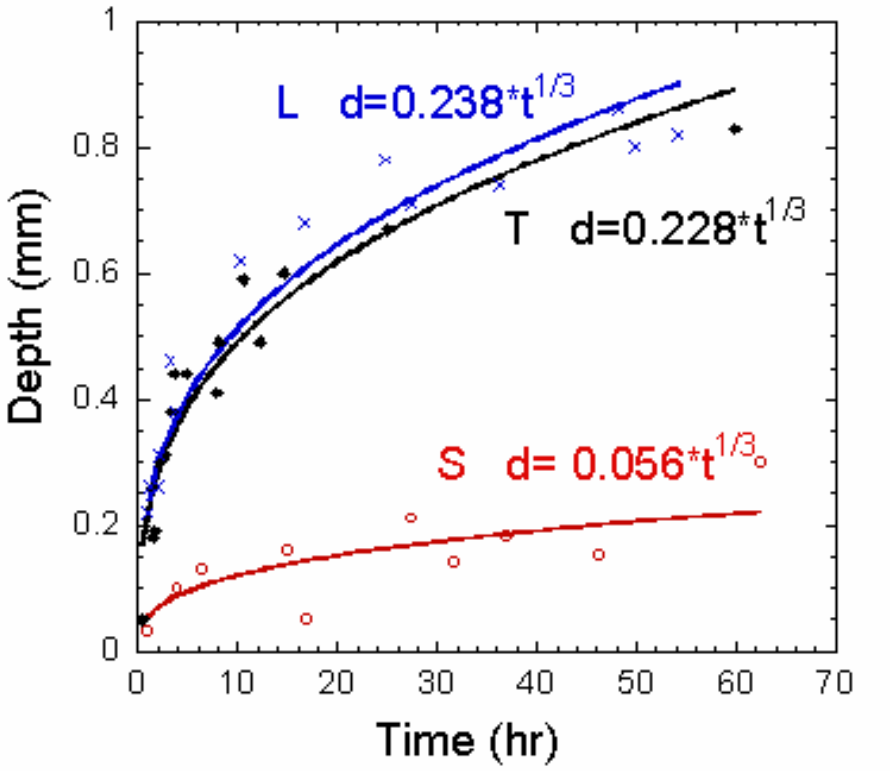

Figure 8. Rate of corrosion penetration by microstructure, from Frankel (3).

When the machining was completed, surface preparation was started. All grease, dirt, and other contaminants were removed before the masking procedure. The specimens were cleaned although the procedure was not described in the reference provided. Masking ensures only the area of interest is subjected to the corrosive compound. The specimens were dipped into MICCROSTOP lacquer, dried, and then a second coat of the lacquer was applied on the edges and corners of the specimen to reduce the chances of preferential corrosion to those areas. The second coat was applied with a Q-tip. The lacquer was chemically removed from the areas to be corroded and the specimen was exposed to 1M NaCl at -700 mV vs SCE (saturated calomel electrode) at "room temperature, with air bubbling, for 42 hours" (see reference 4). The exposure time was based on previous trials with similar depth-of-attack requirements. The Corrosion Kinetics Lab at Ohio State reported the process removed 820 microns on the T surfaces and 862 microns on the L surfaces. Post-failure, broken specimens were serial sectioned to verify this claim.

Specimens were tested with varying material orientations so that fatigue results would be applicable to a variety of locations. The locations and orientations were chosen such that all possible crack nucleating areas around a fastener in a spanwise or chordwise joint were tested. Specimens were corroded on the front (LT), side (LS or ST, considering load direction) or both. Corrosion on the front of the specimen represented corrosion occurring

from the wing skin's contact with the environment, while corrosion on the side of the specimen, along the contour of the hourglass, represented corrosion from contact with the environment and rivet material. A test matrix was developed containing corrosion conditions on the front, side, or both for each loading direction, longitudinal and transverse, with three replicates of each.

The specimens were tested using a load spectrum developed by the Northrop Grumman Corporation (NGC) to simulate the loads experienced on the E-8C upper wing skin. NGC provides maintenance, overhaul, refurbishment, and Aircraft Structural Integrity Program (ASIP) support for the E-8C fleet. The NGC model is a simple wing bending moment calculation. The wing bending moment is zero at the wing tip and maximum at the wing root. The area of interest for this investigation was at WS320; thus, wing bending stresses outboard of WS320 are less than those at WS320. The maximum stress in the spectrum was 16.8 ksi and the minimum stress was -28 ksi; thus, the stress ratio, R, was 1.67. The specimens ran to failure or to the equivalent of two lifetimes. Specimens that did not fail during the first test were then exposed to another, more severe, spectrum that was altered by using a multiplication factor of 1.2 on the tension peaks. Further detail regarding this multiplier will be revealed in the Results section.

One pass of the spectrum, 468,172 cycles, represents 2000 flying hours. The design service goal, one lifetime, of the E-8C is 10,000 hours; thus, to be consistent with MIL-STD-1530B, the fatigue tests were run to two lifetimes, 20,000 hours. Testing to two full lifetimes is conservative since a portion of the fatigue life has been used in service; therefore, the remaining life, 20,000 hours less the current number of hours the aircraft has been flown, would have also been appropriate for fatigue testing.

Ultimately, repair guidance will be given on whether the EC should be repaired or not. According to the E-8C technical order (TO), the KC-135 technical order is commonly used and is the case for the UWS exfoliation corrosion. Exfoliation can be mechanically blended out, can be repaired with a flush mount patch, or the skin can be replaced. A more attractive option in terms of cost and maintaining mission capable rates is to leave the exfoliation until which point the repair can be scheduled within the normal maintenance schedule. Unscheduled, also known as "drop-in", maintenance is more costly to the user than program maintenance. The current effort will address the effect of EC on fatigue life. In parallel efforts, the effects of EC on static stability and bonded repair of corrosion are being investigated.

The corrosion protocol was in its developmental stage at Fontana Corrosion Center when the specimens were prepared, but the lab at OSU had developed a consistent process by that time. The specimens were all Al 7178-T6 and the widths were approximately 12.7 mm at the net section. The specimens were 25.40 mm wide and 76.20 mm in length, as seen in Figure 9. Holes were present in only a few of the specimens provided to allow for *in situ* fatigue testing in a SEM; however this option was not used as the *in situ* SEM fatigue testing only provides surface observations.

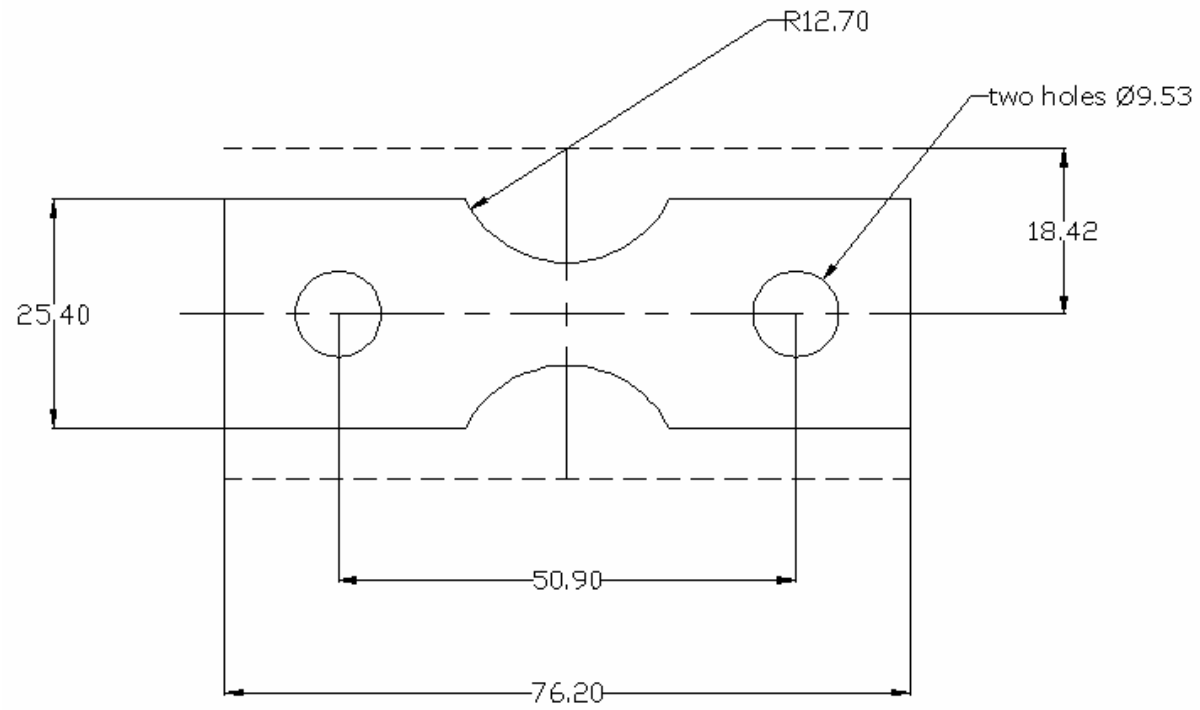

Figure 9. Specimen dimensions in mm.

In a typical specimen of this geometry, the exposure to compressive stress and buckling would be an issue, however, the critical buckling load, using Eqn (1) is over 52 kips. The maximum compression is -1890 lbs when using the spectrum with a minimum stress value of -28 ksi. As a measure of simplicity, the Euler buckling calculation [Beer and Johnston (6)] assumed the narrowest section was present across the entire gage length for both ends being fixed. The effective length (L_e) was chosen given that the specimen would experience fixed-fixed loading condition which replicates the boundary conditions in the fatigue test.

$$P_{cr} = \frac{\pi^2 EI}{L_e^2} \tag{1}$$

where E = 10500 ksi

$I = \frac{bh^3}{12}$ and b = 0.45” and h = 0.15”

and

L_e = ½ L

In addition to loading direction, each of the corrosion conditions added variability. This can be seen in Figure 10 with material orientation coordinates. There were no un-corroded specimens tested as the loading spectrum was too benign to nucleate a crack from a pristine specimen. The target corroded depth of the material was 30% of the specimen thickness since this is the limiting depth as called out in the TO.

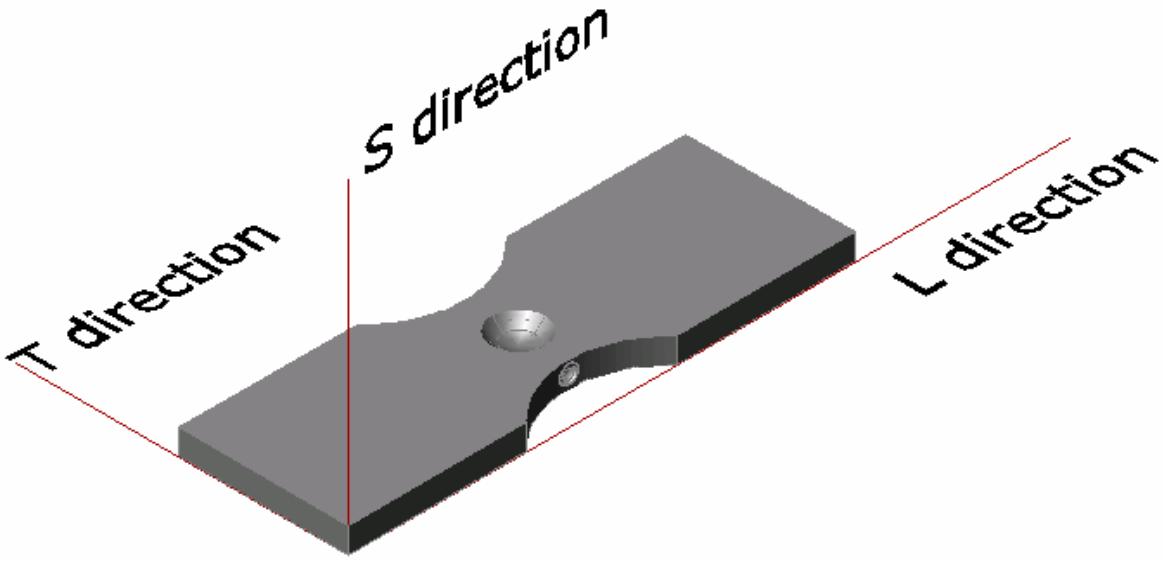

Figure 10. Specimen in three dimensions showing loading the same as the longitudinal direction with corrosion on LS and LT faces.

Each of the geometries and each corroded condition with three replicates of each yielded a total of 18 specimens. These are outlined in Table 2.

Table 2. Specimen geometry and location of corrosion sites, noted with quantity of each.

	LT	*LS*	*LTLS*	*ST*	*LTST*
loading in L direction (spanwise)	3	3	3	0	0
loading in T direction (chordwise)	3	0	0	3	3

The specimens were analyzed post-test to determine the crack nucleation location and size by use of a scanning electron microscope (SEM). Measurement of the corroded area on the fracture surface was observed via an optical microscope and a serial sectioning procedure. Serial sectioning is a method that helps determine the specimen topography by repeating a polishing process and measuring the area of each polished surface. This idea of slicing can be seen in Figure 11.

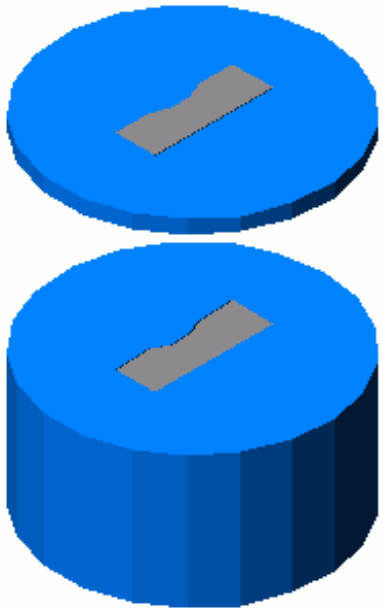

Figure 11. Schematic showing process of removing layers in serial sectioning to expose entire specimen for measuring topography.

This time-consuming method was useful in that the three-dimensional corrosion damage was measured. Further discussion follows.

Steps for the Entire Experimental Investigation

1. Before Fatigue Testing

The electrochemical corrosive compound could remain active due to the inability to remove chemicals from the intergranular fissures in the specimen; therefore, the specimens were stored in a freezer (at approximately -40º F) to minimize the chance that the corrosion process would continue. As another measure of protection, specimens were stored in individually sealed bags to prevent further surface damage. When a specimen was to be tested, it was removed from the freezer and placed in a desiccator for at least two hours to allow warming to room temperature without condensation build-up. In order for the corrosion compound to be reactivated, the fatigue tests were completed in an environment of 100% relative humidity. The ambient temperature was 76ºF. Specimens were loaded into the test frame after being surrounded by wet paper towels and sealed inside of a plastic bag. Sufficient humidity levels were visually verified by the noticeable heavy condensation inside the bag as seen in Figure 12**.** A hygrometer was used initially, and readings were at about 95% consistently. After the first couple of specimens tested, it seemed useless to measure humidity when visual examination was a good measure alone.

Figure 12. Specimen under fatigue testing in high RH environment

2. Fatigue Testing

The fatigue testing was completed using MTS and SATEC closed-loop, computer controlled, servo-hydraulic test frames of varying load capacities. The MTS TestStar IIm software was used to control the test frames. The capacities of the test frames varied from 10 kips to 55 kips. The tests were controlled by the loading rate which provides better correlation between the load command and response signal. The maximum loading rate that can be achieved, without sacrificing accuracy, by each machine is a function of the machine capacity. As can be seen in Table 3, the frequency varies with machine capacity. Most tests were performed on the two smaller capacity MTS frames shown in Table 3. No crack growth monitoring was used as this was a stress-life test.

Table 3. Load capacity and average frequency of each while running the full E-8 UWS spectrum.

Brand	Load Capacity (kips)	frequency (Hz)
MTS	10	15.5
MTS	11	13.6
MTS	55	7.8
SATEC	20	2.8
SATEC	50	2.4

3. SEM Analysis

Scanning Electron Microscopy was performed on failed specimens to determine the nucleation site and size for each. Prior to being placed in the scanning electron microscope (SEM), the specimens were carefully cleaned in a bath of acetone in an ultrasonic cleaner, then in another bath of isopropyl alcohol in the ultrasonic cleaner. Each cleaning process

was performed for approximately two minutes. After cleaning, the specimens were mounted on a specimen stage using black conductive tape. Careful to not expose the cleaned, mounted specimens to dirt or oil, the specimens were placed in the vacuum chamber of the SEM, ready for analysis.

The Cambridge Stereoscan 250 was set to 20kV during the analysis, as this is typical for viewing fractographic aluminum surfaces. The analysis began at about 20x and was increased as necessary. With each magnification, different focusing methods were used and levels of brightness and contrast were changed accordingly. Secondary and backscatter modes were used to capture different aspects of the same image. Backscatter mode is commonly used to find second phase particles. The images from the SEM were recorded using imaging software called Orion.

4. Serial Sectioning

Serial sectioning was done after testing on one half of the fractured specimen to confirm the amount of corrosion at the fracture plane was approximately 30%. The serial sectioning process is destructive, so analysis in the SEM and via optical microscopy was performed first. A set of essential tools existed in the lab that was used for this process including a phenolic molding machine, a mechanical polisher, and an optical microscope with image analysis capabilities (Omnimet was used here). These instruments are readily available for basic metallurgical studies.

The molding machine used a disk of phenolic material with a stand (or clip) in conjunction with pressure and temperature to completely encase the specimen into the mold. The mold was necessary to hold the specimen in a fixed position so that measurements could be compared accurately. For instance, a skewed placement under the microscope may result in varying or non-repeatable surface measurements. To ensure a proper angle in the mold would be maintained, a clip was used as a stand. Also, the mold created a simple means for measuring the thickness polished off during successive removal of thin amounts of specimen and mold. Polishing removes small amounts at a time. Polishing was deemed an easy method to mechanically perform material removal in precise amounts. To obtain consistent thickness removal, the amount of time on the polisher and the paper grit were determined on earlier specimens by trial and error. The polisher faced off material for approximately every 200 μm (0.008 inches was the target removal). This amount was decided upon from previous serial sectioning experience. Using smaller increments than that is not necessary as higher resolution results could be interpolated from the 200 μm increments. Using thickness increments more than that proved to have a significantly larger error than those with smaller increments.

Images were recorded at approximately 7.5x. An image that is representative of how the area is calculated can be seen in Figure 13.

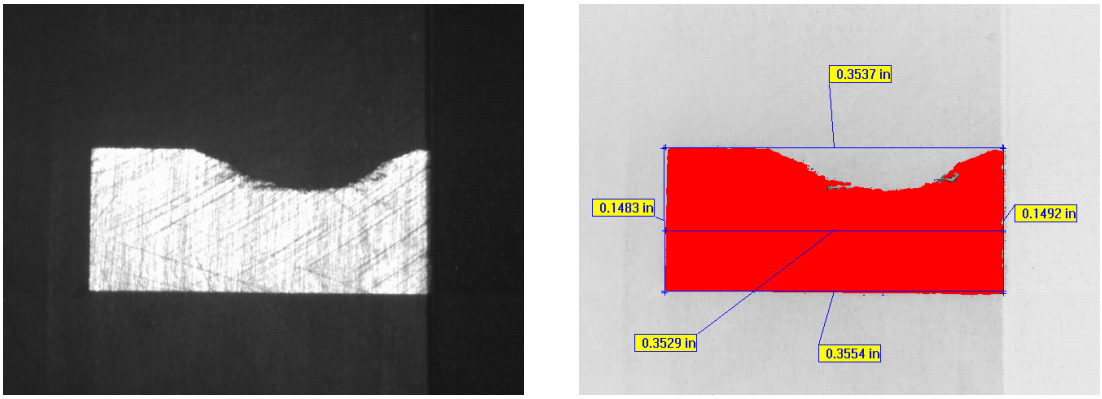

a. **b.**

Figure 14. a. Image captured from Omnimet; b. image captured with manual measurements for area analysis. The measurements shown are used in later analysis to find amount of area lost due to corrosion. The area found on Omnimet is subtracted from the calculated pristine area.

This magnification was the default in the image analysis software and gave acceptable resolution. The software program used was automatically calibrated for length at its preset magnification. Thickness and length readings were measured directly over the image of the specimen. The lengths were averaged and the thicknesses were averaged in order to calculate a pristine cross-sectional area. The amount of material removed and the depth of removal were the parameters of interest. The image analysis software contained a programming tool that allows setting the threshold brightness limit for each image. Since the mold was black and the specimen was quite reflective under the optical microscope's light, the threshold value was not difficult to find. This amount of brightness was set and upon completion of the program, the image of the specimen would appear to be colored over while the mold would retain its original color. See Figure 11 for an image simulating the serial sectioning process. The software program could then calculate the area of the shaded region. This number could then be compared to the manually calculated area to find the area loss due to corrosion. For each of the removed thicknesses, the amount of volume loss was calculated by multiplying the surface area lost by the thickness removed. The process is quite time consuming as each specimen was polished up to the point where corrosion no longer existed.

4. Results

The fatigue testing was comprised of two parts; the first portion of the test was completed using the original load spectrum from Northrop Grumman (approximately 9.37 million cycles in total simulating two aircraft lifetimes). Since none of the specimens failed during the first portion of testing, a second part was used to test cycles to failure. The upper wing skin load spectrum used was compression-dominated. In order to increase the likelihood of crack nucleation, a multiplier of 1.2 was used on the tension peaks in the original spectrum. This increase was determined to significantly reduce the number of cycles to failure without using data that is far from actual service loads.

Of the eighteen specimens tested, fifteen useful data points were obtained. No data was collected for three specimens that were damaged by testing anomalies. In Table 4**,** the results are listed by orientation and corrosion location, along with the result of two sets of fatigue tests. The cycles to failure are listed per condition in Table 5**.**

Table 4. Specimen result after completion of second load spectrum

Loading Direction "L"				Loading Direction "T"			
	failed	no failure	no data		failed	no failure	no data
LTLS	2	1	0	*LTST*	3	0	0
LT	1	1	1	*LT*	0	3	0
LS	0	2	1	*ST*	1	1	1

Table 5. Number of cycles to failure during second, more severe, load spectrum where letters in subscript correspond to details regarding crack nucleation site.

Loading Direction "L"		Loading Direction "T"	
	failed (N_f)		failed (N_f)
LTLS	$2{,}740{,}914_a$ $7{,}157{,}886_b$	*LTST*	$4{,}644{,}128_d$ $5{,}120{,}304_e$ $9{,}192{,}452_f$
LT	$6{,}015{,}498_c$	*LT*	
LS		*ST*	$3{,}251{,}101_g$

a. *The crack nucleated away from both corrosion sites at an "L" shape away from free surfaces. It seems as if the specimen experienced inadvertent shear loading in the test frame. See* Figure 29 *through* Figure 32.
b. *The crack here nucleated between corrosion on the side and on the front of the specimen. This area would be likely for failure due to the surrounding weakened ligaments. See* Figure 16 *through* Figure 20.
c. *This specimen had no corrosion on either side, yet it nucleated on the side of the specimen, most likely due to the K_t of the specimen design. See* Figure 33 *and* Figure 34.
d. *Corrosion conditions were on the front and side of the specimen and nucleated where expected—at the side of the specimen where corrosion existed. See* Figure 35.

e. Nucleation seemed to be caused at the corner of the specimen between corrosion sites. Again, reason for this may be explained by the weakened surrounding material. See Figure 21 *through* Figure 23.

f. This nucleation occurred away from the most susceptible corner, but it corrosion was not apparently a factor. See Figure 24 *through* Figure 26.

g. This specimen had corrosion only on the side and corrosion seems to be the cause for this failure as beach marks are present which have formed circumferentially to the corrosion. See Figure 27 *and* Figure 28.

The serial sectioning process revealed that on average, the corrosion seen on the LT faces was very close to 30% with a maximum depth read at 32% of the thickness. Table 6 displays the amount of material lost on each plane. For analysis, the depth of corrosion on the side of the specimen was normalized for width and the depth of corrosion on the front of the specimen was normalized for the thickness. It was obvious after fracture, though, that the other planes did not have such deep damage. In fact, of four specimens with corrosion on the ST and LS planes, the percentage thickness losses were 3.8% for ST and 2.8%, 3.4%, and 4.7% (for LS planes).

Table 6. Depth of corrosion of various specimens and the corresponding faces

loading direction	corrosion face	corrosion face
L	LS, 3.3	
T	LT, 29.4	ST, 7.2
T	LT, 31.0	ST, 5.7
T	LT, 30.3	ST, 3.8
L	LS, 2.8	
L	LT, 32	LS, 3.4
L	LT, 29.3	LS, 4.7

Considering the number of cycles that most of the specimens completed, it is possible that not all the failures were nucleated by corrosion damage. This was obvious after visual observation of at least one specimen. After specimen failure, a beach mark is visible at a macroscopic level and is representative of where a fatigue crack most likely nucleates. Beach marks form radial lines in the fatigued zone of the fracture. Crack initiation sites are at the center of the radius of curvature of the beach marks. They are generally easy to see as the luster is different than the rest of the fracture surface and it is a relatively flat area. Figure 15 shows beach mark indicating that nucleation occurred where corrosion did not exist. This specimen had been corroded on the LT face under loading in the L-direction. The mark is usually in the shape of a semi-circle with its center referring to the nucleation site. The outermost part of the mark is formed by the crack growth front. Although striations were clear in a few of the fracture surfaces, due to the almost random nature of the load spectrum, predicting a crack growth rate would be of little value.

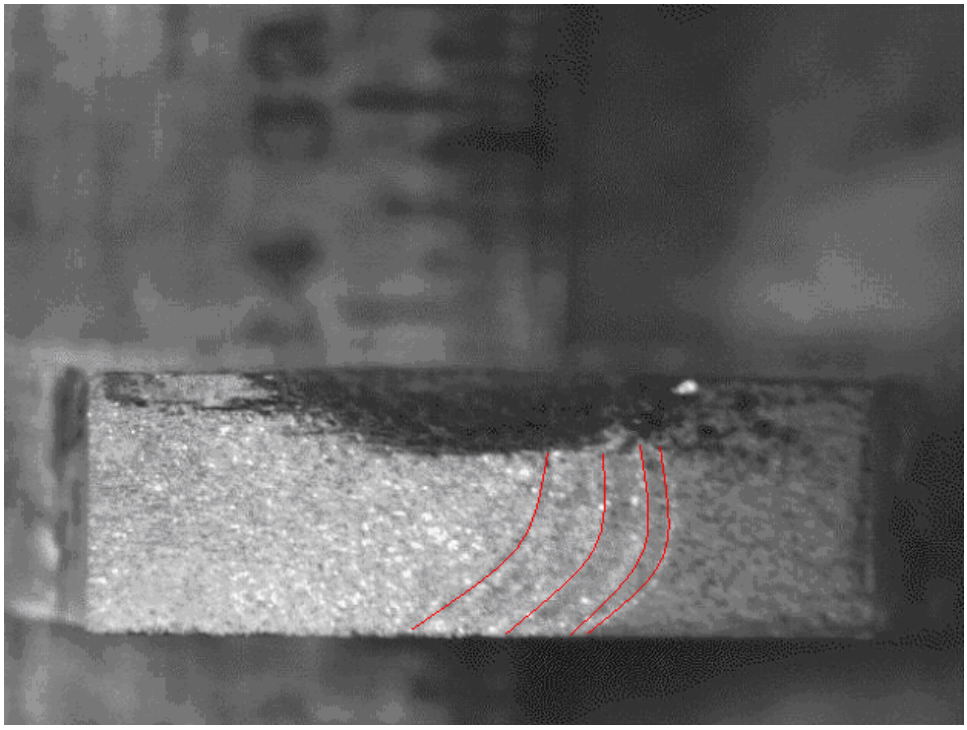

Figure 15. Specimen loaded in L direction with corrosion only on LT plane. Beach mark is the brighter part of the fracture surface and red marks help to enhance the crack growth bands. Scale marks in 1/64".

The corrosion did not seem to cause nucleation in all the specimens, as can be seen in Figure 15 above. Although IC emanates from the pit on the LT plane (in the longitudinal direction) in both directions, the area of IC that seemed less severe was in the area where the crack nucleated. The cause for nucleation in the corner of the specimen is most likely due to the stress concentration factor from the IC combined with the location (the corner of the specimen). Images from the optical microscope and from the SEM can be seen for each fracture surface in Figure 16 through Figure 34.

SEM Analysis of Specimens

Intergranular corrosion was the cause for another fatigue crack nucleation. One of the specimens loaded in the L direction with corrosion on both faces clearly nucleated from IC on the side of the specimen. See Figure 16. Specimen 1 may be referenced here. Another specimen with similar failure was the second replicate of corrosion on both locations with loading in the T direction. The nucleation occurred where the specimen is most likely the weakest—the corner between the "side" and "front" corrosion.

1. **Specimen loaded in L direction with corrosion on LT and LS planes, replicate number one.**

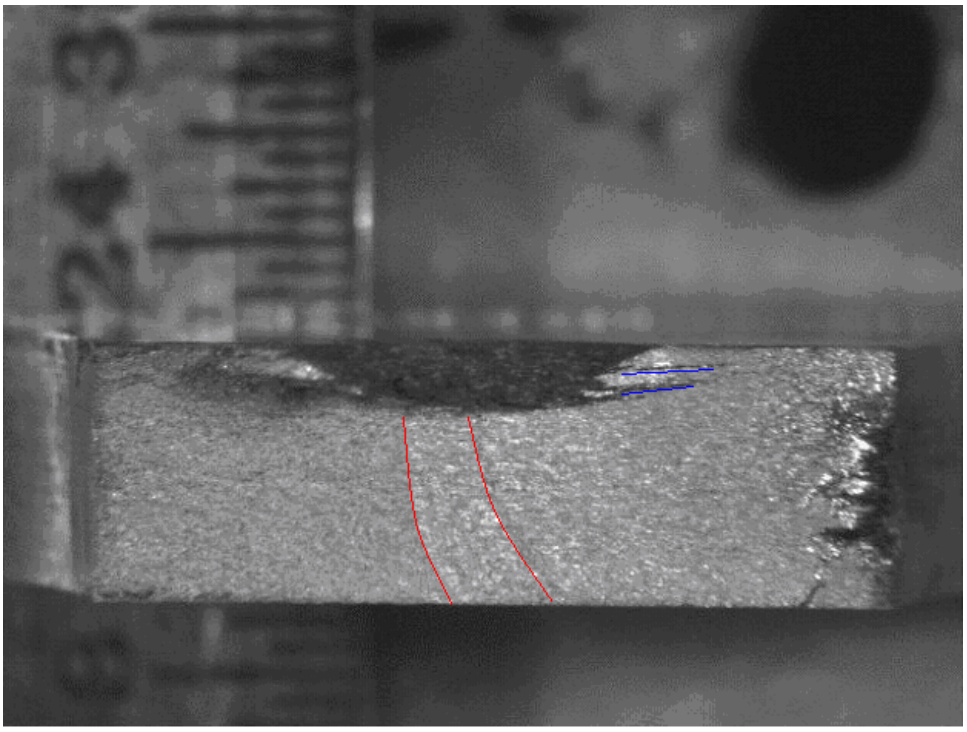

Figure 16. Optical microscope used to capture entire image of specimen. Magnification is about 7.5x with scale marks of 1/64-inch. Severe intergranular corrosion highlighted in blue can be seen from the left side of the corrosion on the LT plane. Also, crack growth bands are visible originating from the right side of the specimen, in red.

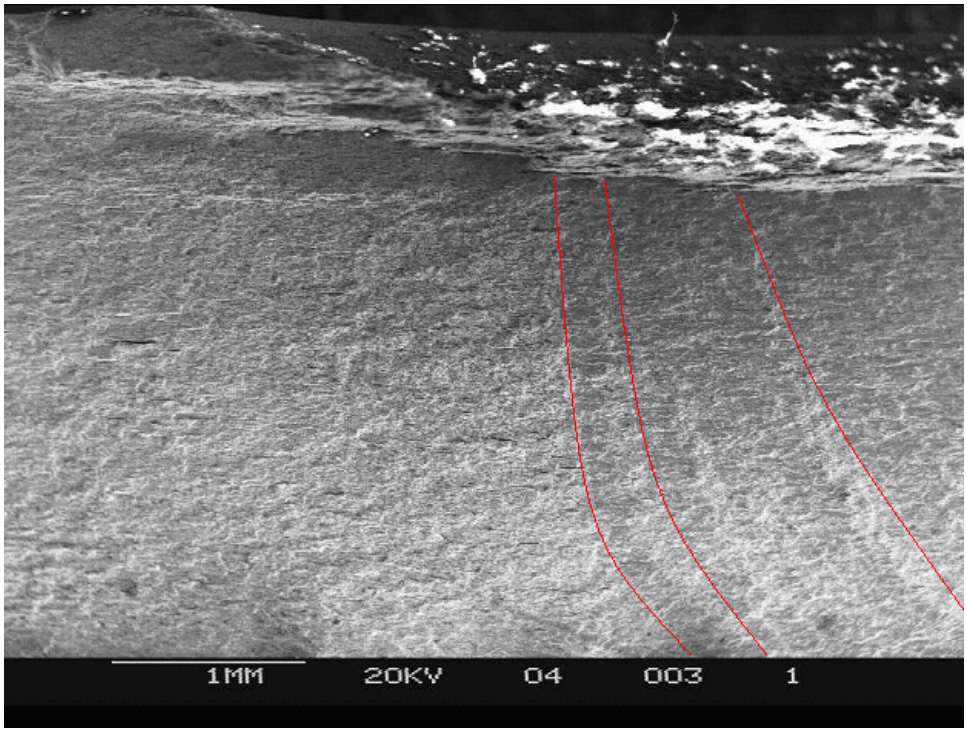

Figure 17. Central region of specimen with 20x in secondary mode to emphasize growth bands. No discontinuities along the corrosion surface seemed to be the cause for crack growth arrest, which leads to the assumption that the crack growth was in its final stage here before failure.

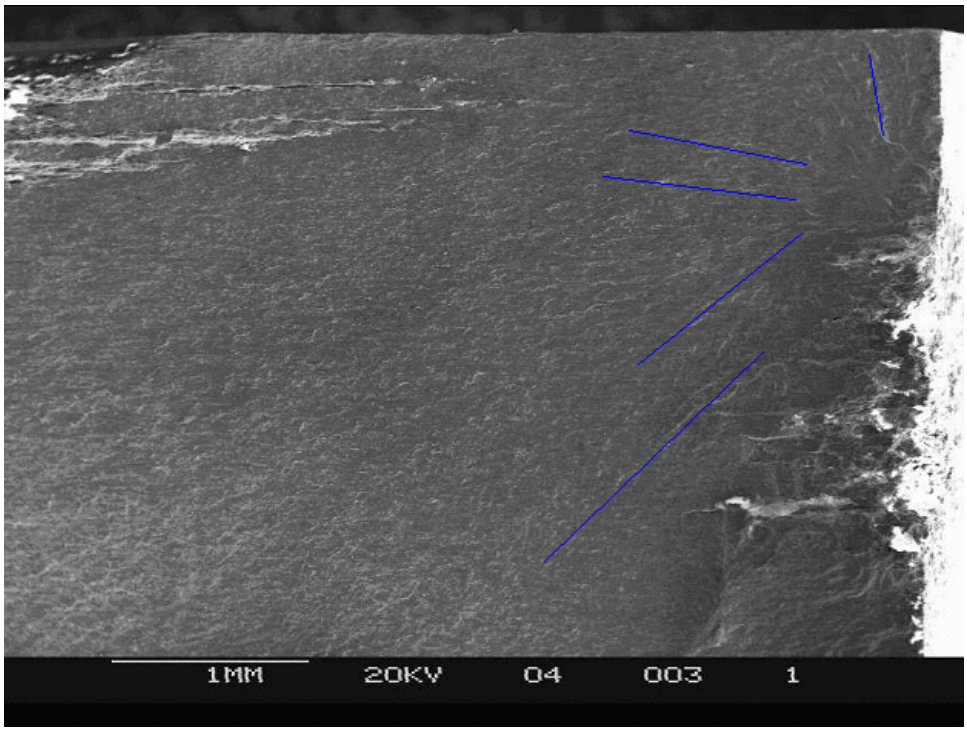

Figure 18. SEM image in secondary mode at 20x. Blue radial lines follow the path of river bands that literally point to the nucleation site.

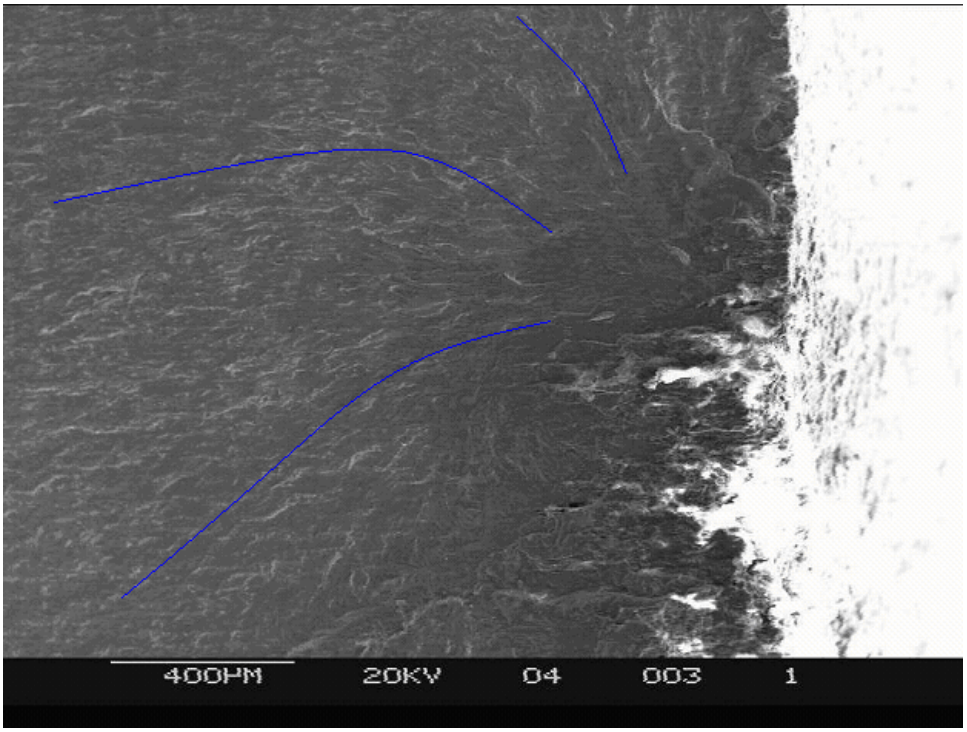

Figure 19. A SEM image of nucleation site at 50x in secondary mode. The nucleation occurs from extreme intergranular corrosion on the LS plane. Blue lines again follow the river bands to point to the nucleation site.

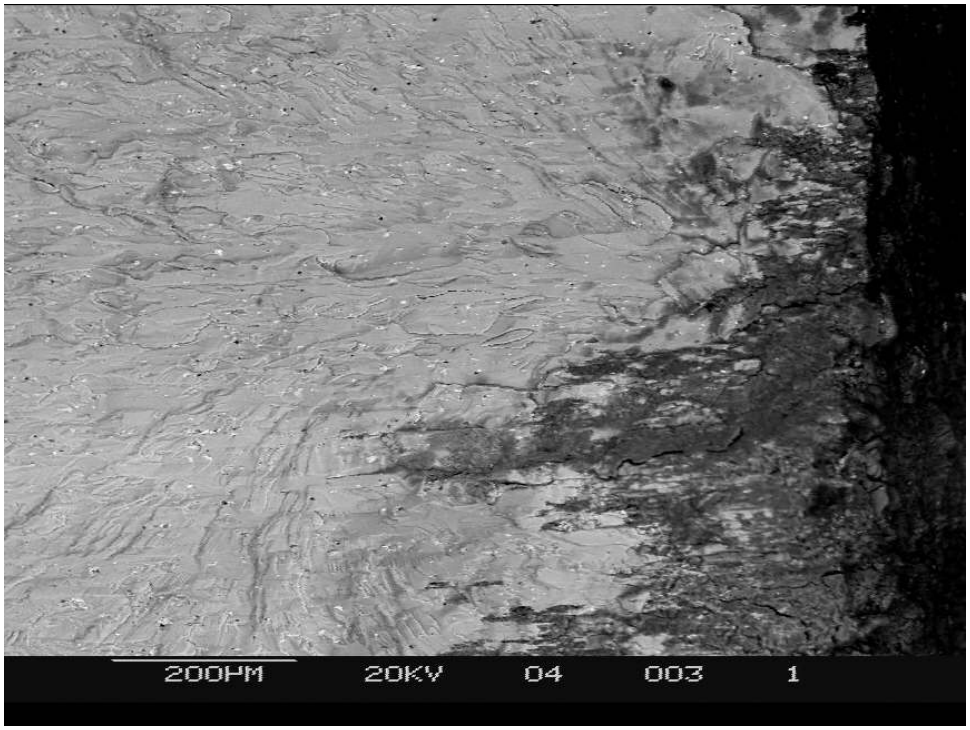

Figure 20. SEM image in back scatter mode at 100x to determine if there were any abnormal particles that may have caused nucleation at this site. Nothing irregular was found; therefore the nucleation most likely occurred from a stress concentration from corrosion.

Severe IC exists away from the nucleation site on the LT face, which implies this did not contribute to nucleation. This may be referenced in Specimen 2.

2. Specimen loaded in T direction with corrosion on LT and ST planes, replicate number two.

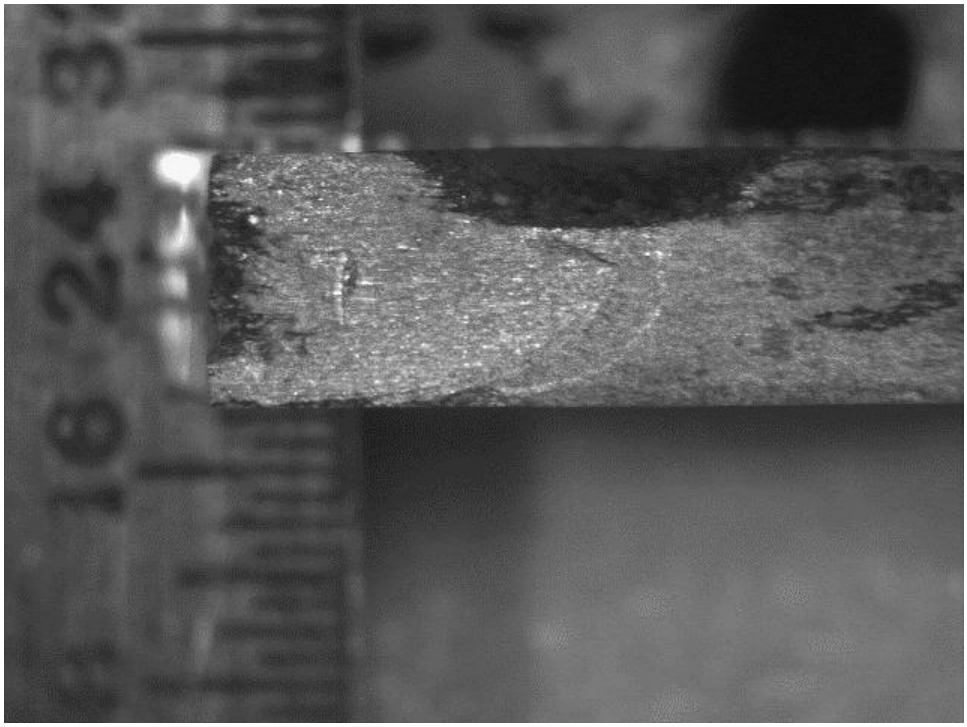

Figure 21. Optical micrograph at 7.5x with scale marks of 1/64-inch. Nucleation clearly occurred on the left side of the specimen from a stress concentration caused by corrosion.

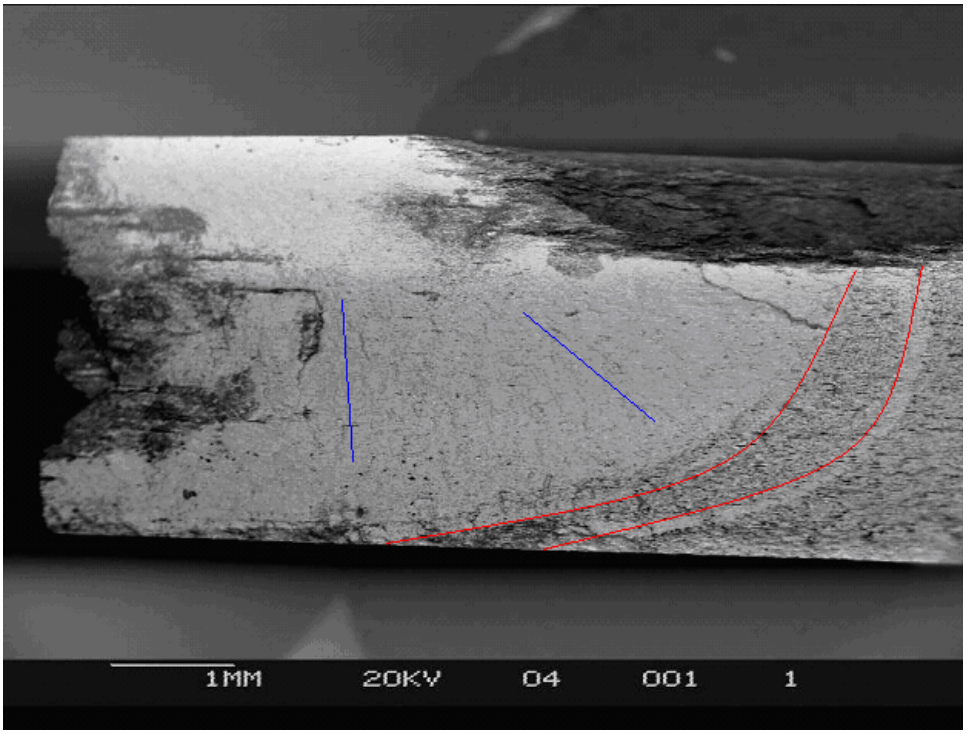

Figure 22. SEM image of left side of specimen where nucleation occurred. Image in back scatter mode and at 12x. Radial lines pointing to crack nucleation site are outlined in blue. Crack growth bands which are circumferential to the nucleation site are shown in red.

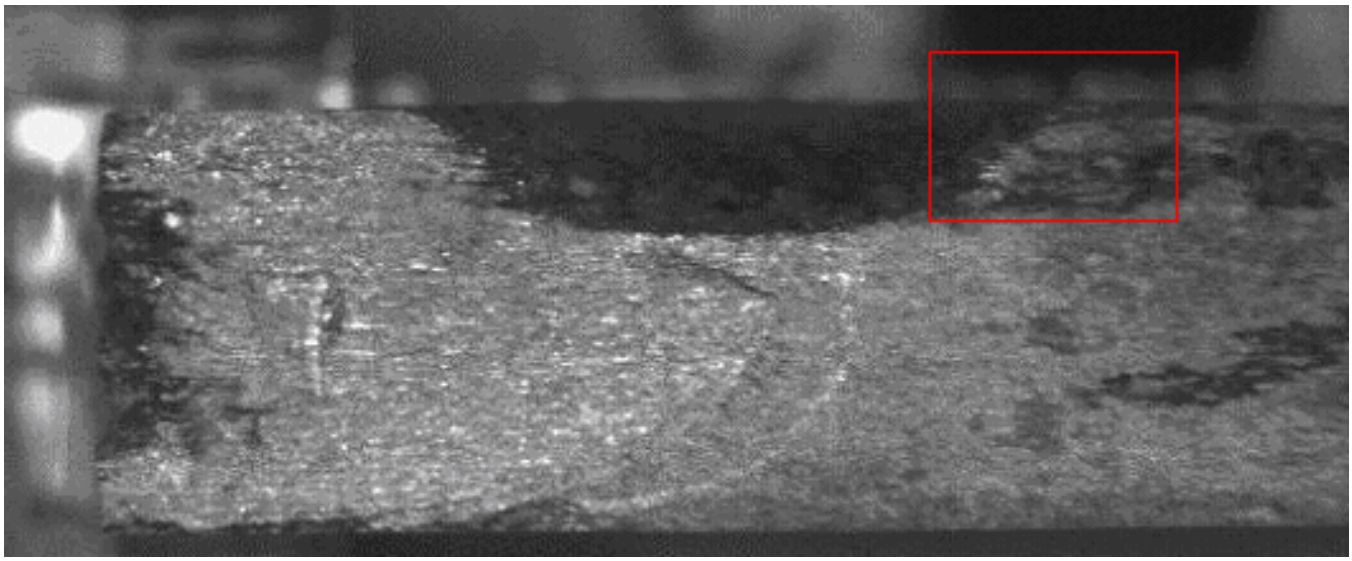

a.

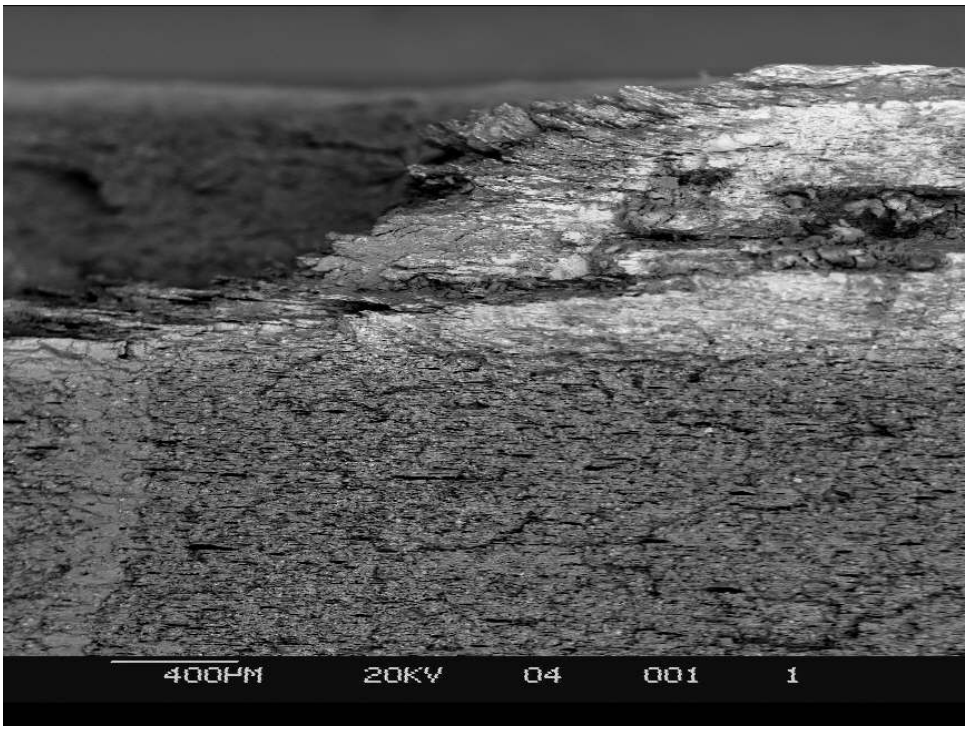

b.

Figure 23. Portion of corrosion on LT plane where severe exfoliation occurred. (Figure a, directly above shows entire specimen with location of this micrograph.) Picture is taken in back scatter mode to detect any abnormalities in the material structure, which was not apparent. The picture was taken in the SEM at 35x.

Multiple nucleation sites occurred on the third replicate of the specimen with transverse loading and corrosion on both faces, on Specimen 3. One nucleation site was at the weakest location which was comparable to the aforementioned Specimen 2. The larger (and more primary) site exists on the LT corrosion site with IC. The beach mark hinting nucleation at this condition is much larger, leading to the assumption this was the primary nucleation site.

3. **Specimen loaded in T direction with corrosion on LT and ST planes, replicate number three.**

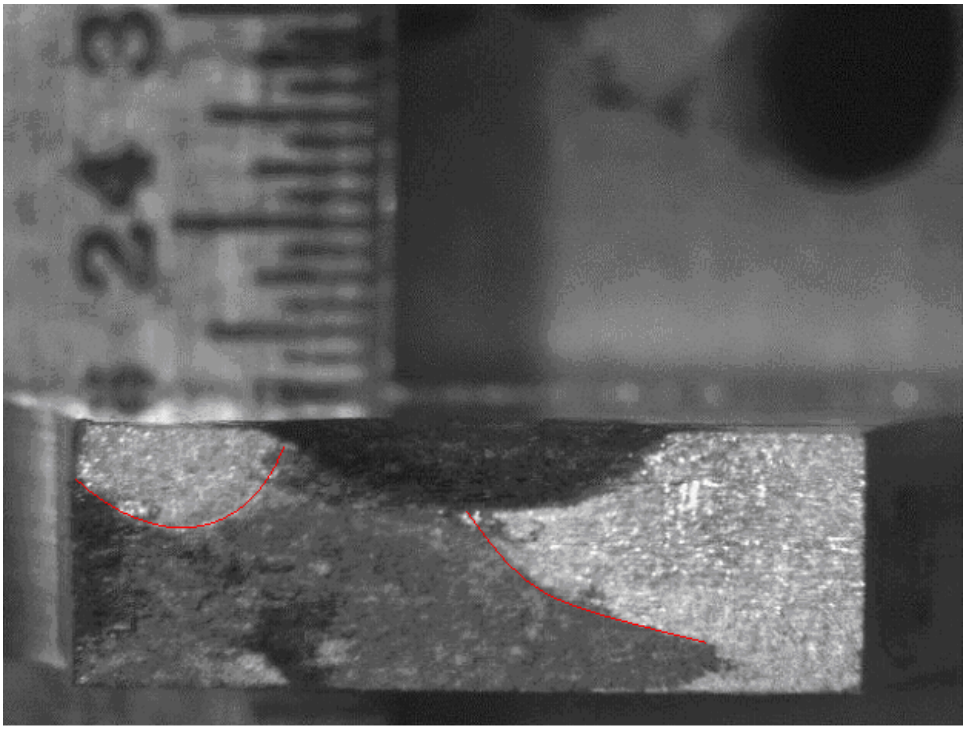

Figure 24. Optical microscopy at 7.5x with scale marks of 1/64-inch. The two shinier regions on the image are beach marks, which are outlined in red, and exist in two areas.

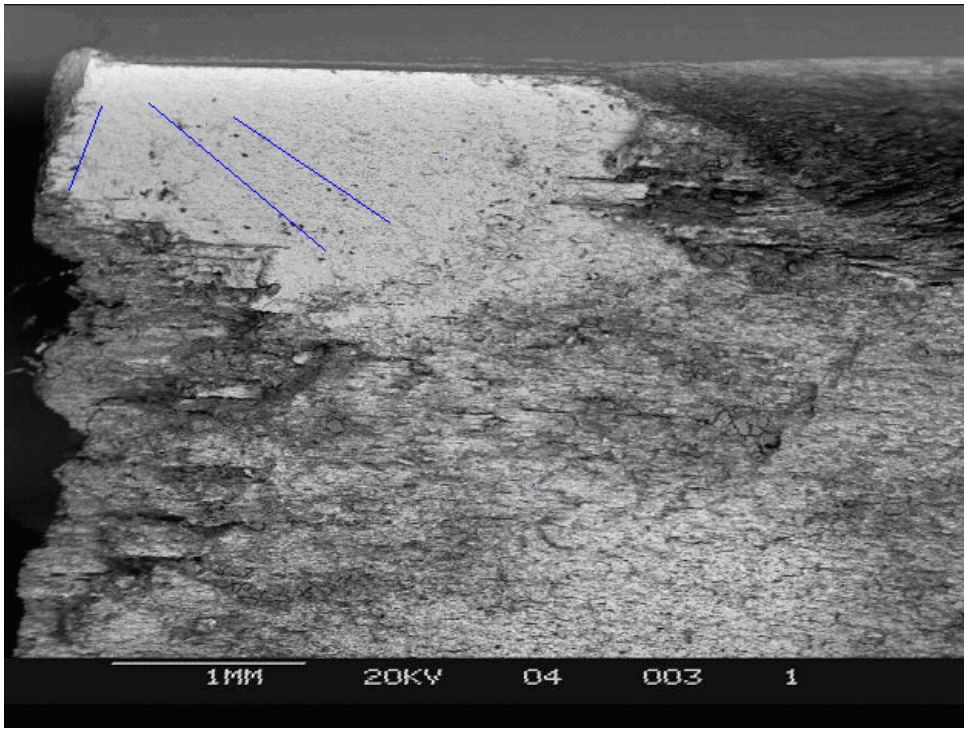

Figure 25. SEM micrograph of corner nucleation site at 20x in back scatter mode. River bands are indicated in blue. The area was a likely site for nucleation since two surrounding areas had severe damage.

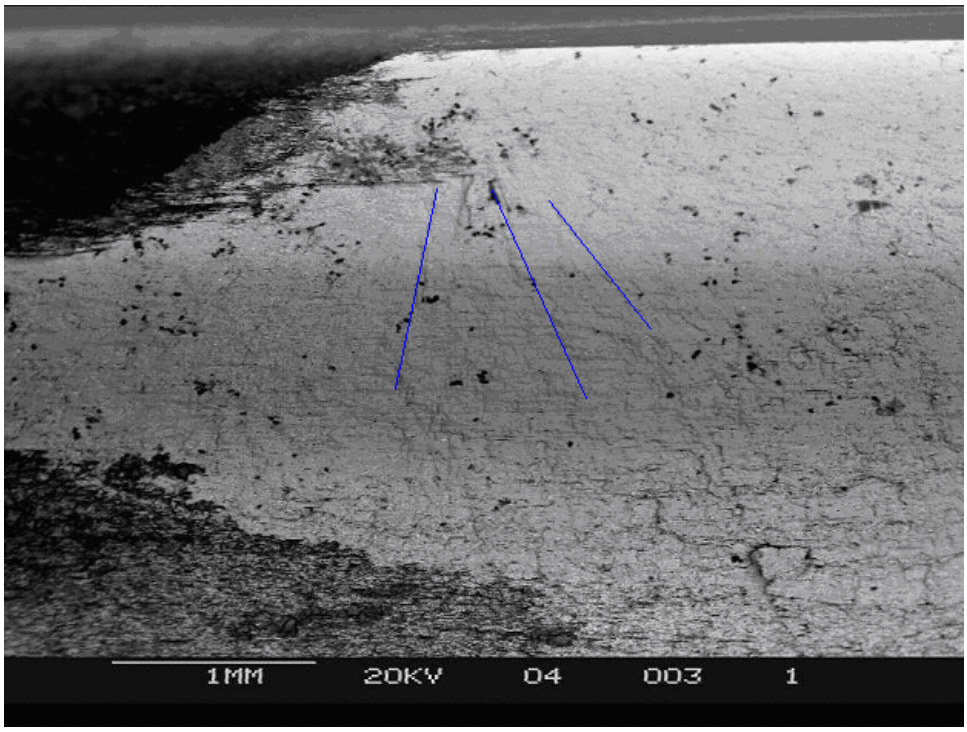

Figure 26. SEM image in back scatter mode at 20x. The initiation site is to the right of the corrosion on the LT plane. The extra intergranular corrosion is most likely the stress concentration factor that caused the nucleation site there.

Replicate number one for the specimen loaded in the T direction with corrosion on the side (Specimen 4) nucleated where predicted—at the nucleation site (on the contoured side of the hourglass). Severe IC emanates from this pit, so the K_t of the specimen geometry or the corrosion could be causes for failure.

4. Specimen loaded in T direction with corrosion on ST plane, replicate number one.

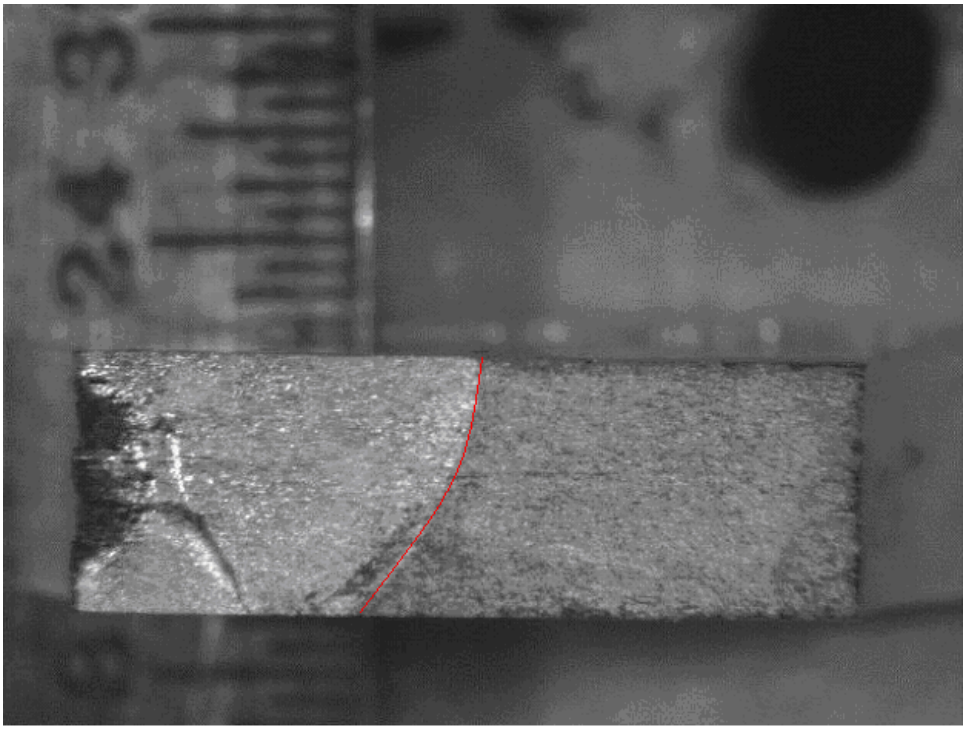

Figure 27. Optical microscope image of specimen, magnification is 7.5x with scale marks of 1/64-inch. Severe intergranular corrosion marks emanating from corroded area. The beach mark covers almost half of the specimen and is outlined in red.

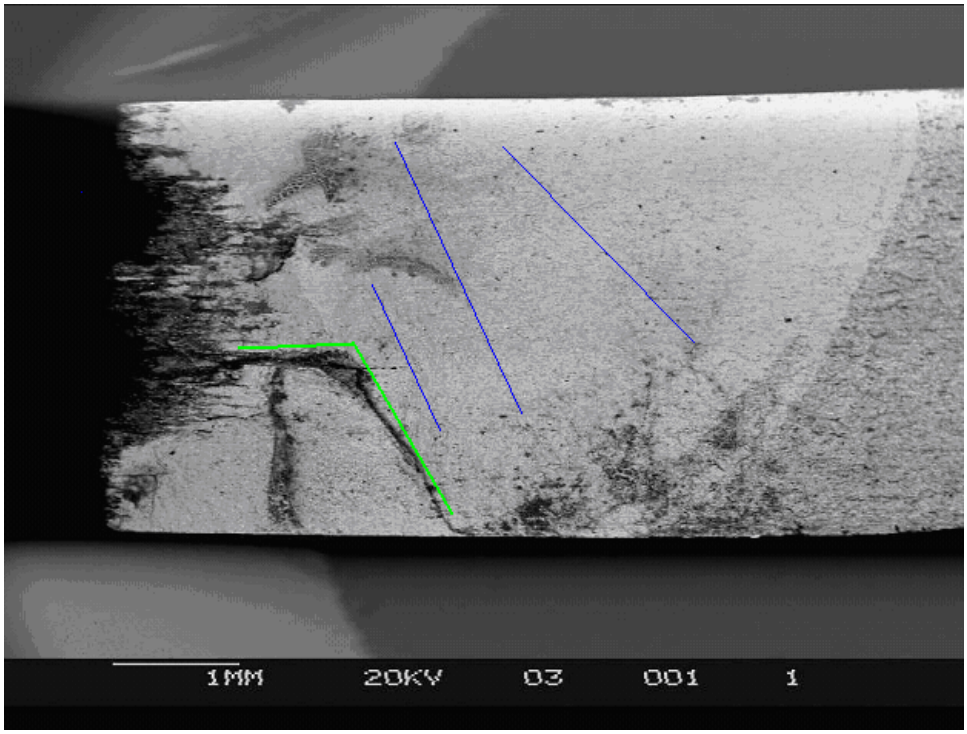

Figure 28. SEM image in back scatter mode at 13x. Corrosion on side of specimen with river bands in blue pointing toward a non-corroded area. The area on the lower left side of the picture is outlined in green and indicates a change of topography. This indicates shear on the fracture surface, perhaps caused by asymmetric loading in the test frame. Note it is not a likely cause for nucleation.

Specimen 5 has an interesting nucleation site. The specimen was loaded in the L direction with corrosion on both faces and was replicate number three. While the specimen had the "weak corner" condition as did specimens two and three, nucleation did not occur there. Instead, a planar crack caused nucleation within the material. This phenomenon was seen in the referenced report to the FAA (reference 8), also.

5. **Specimen loaded in L direction with corrosion on LT and LS planes, replicate number three.**

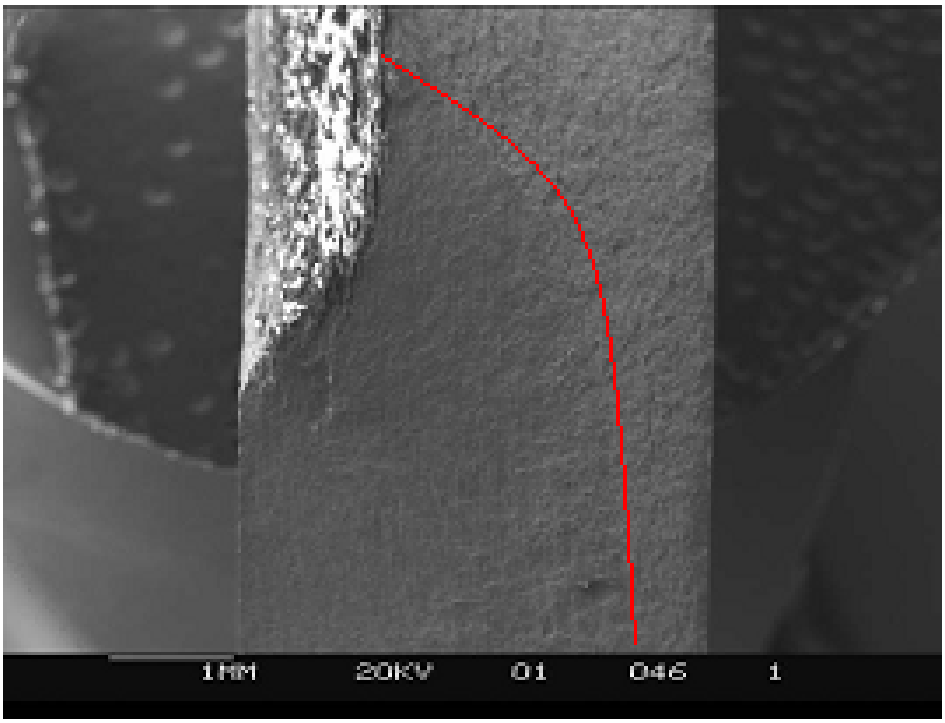

Figure 29. Corroded area on front of specimen; bottom portion of specimen shows beach mark, 20x in secondary mode. The red follows the border slightly outside of the beach mark.

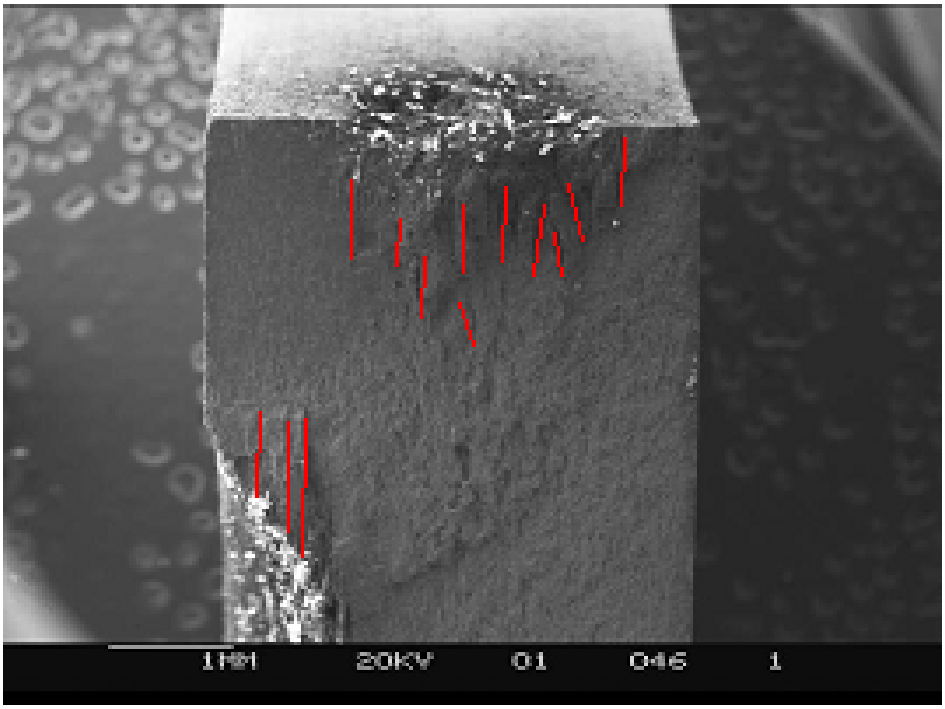

Figure 30. Top portion shows another corroded area with inter-granular corrosion, 20x in secondary mode. IGC is emphasized with red.

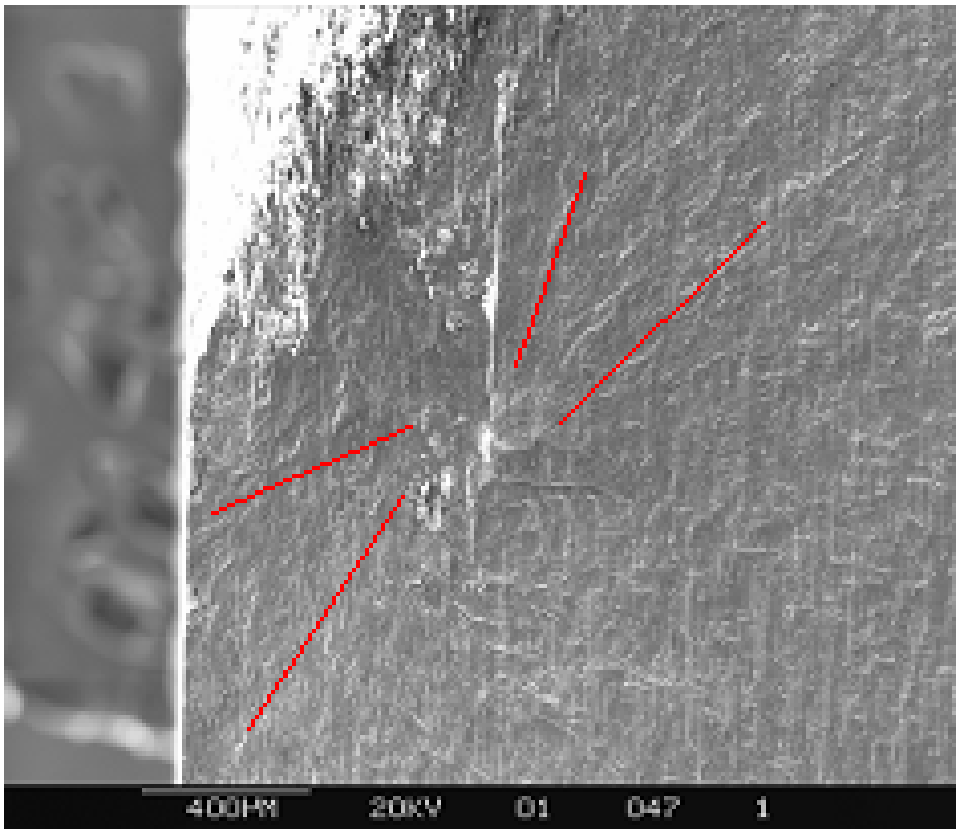

Figure 31. Under corroded area on front with L shape nucleating feature, 50x in secondary mode.

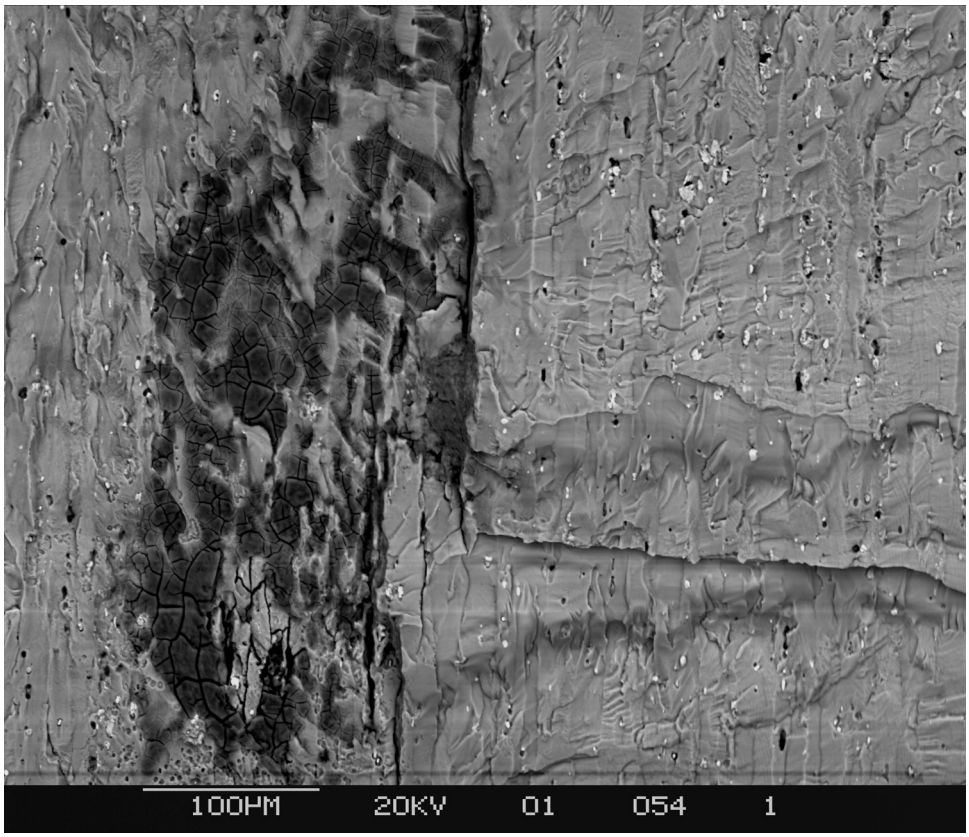

Figure 32. L-shape nucleation, 200x in back scatter. The vertical portion of the shape follows the grain boundaries, while the other part of the formation might have been caused by shear. Asymmetry in the test frame may have been to blame. The black marks in backscatter mode indicate no material abnormalities, hence this was not a cause for nucleation.

The side, like many of the other specimens, was the nucleation site for Specimen 6. The specimen was loaded in the L direction with corrosion on the front and was replicate number one. There was no indication for a cause of nucleation at this location, except the specimen geometry. Also, crack growth bands are evident about half of the way across the specimen, but these are not helpful when determining crack growth rate due to the type of load spectrum used.

6. Specimen loaded in L direction with corrosion on the LT plane, replicate number one.

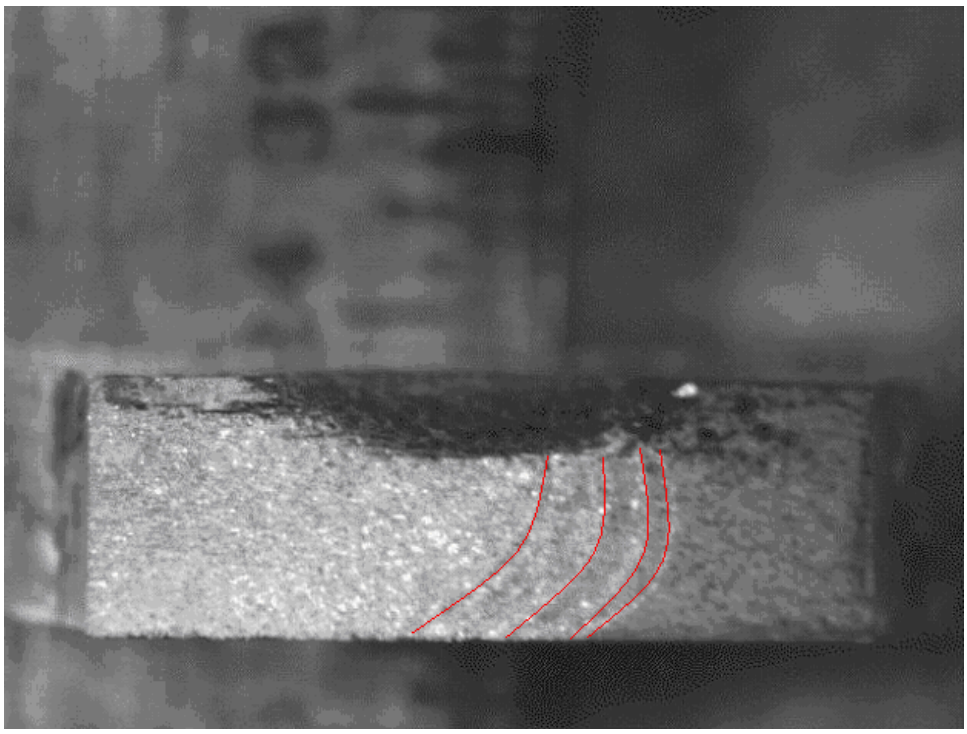

Figure 33. Specimen loaded in L direction with corrosion on LT plane. 7.5x optical magnification with scale in 1/64-inch increments. Red lines identify beach marks which indicate a nucleation site on the left side of the specimen—away from corrosion altogether.

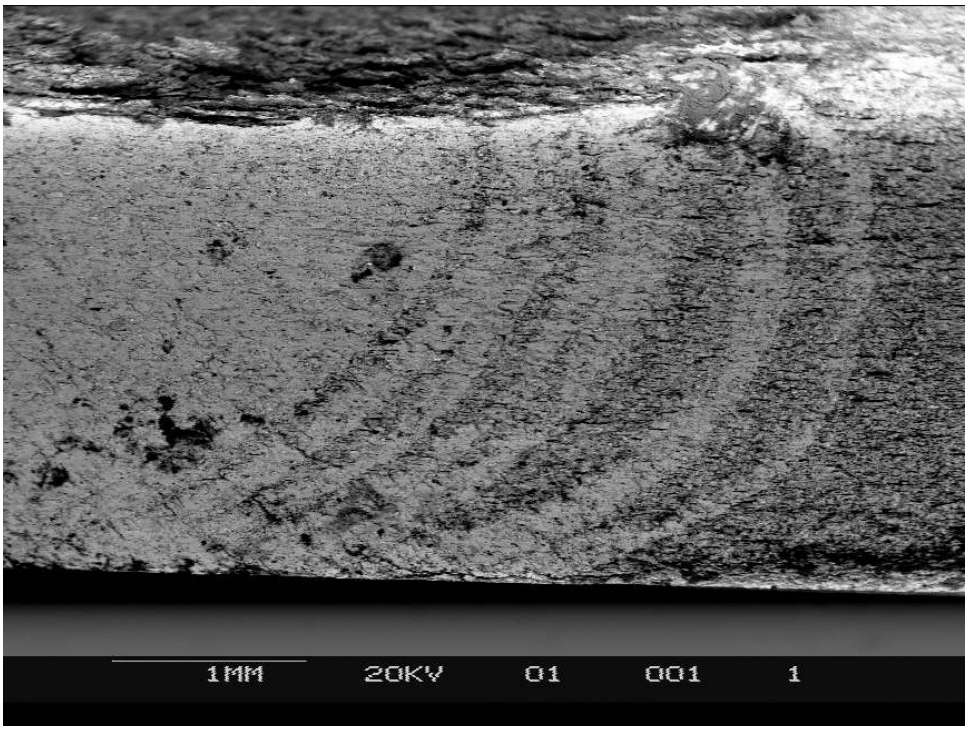

Figure 34. SEM image of crack growth bands; 20x magnification in back scatter mode.

7. Specimen loaded in T direction with corrosion on LT and ST planes, replicate number one.

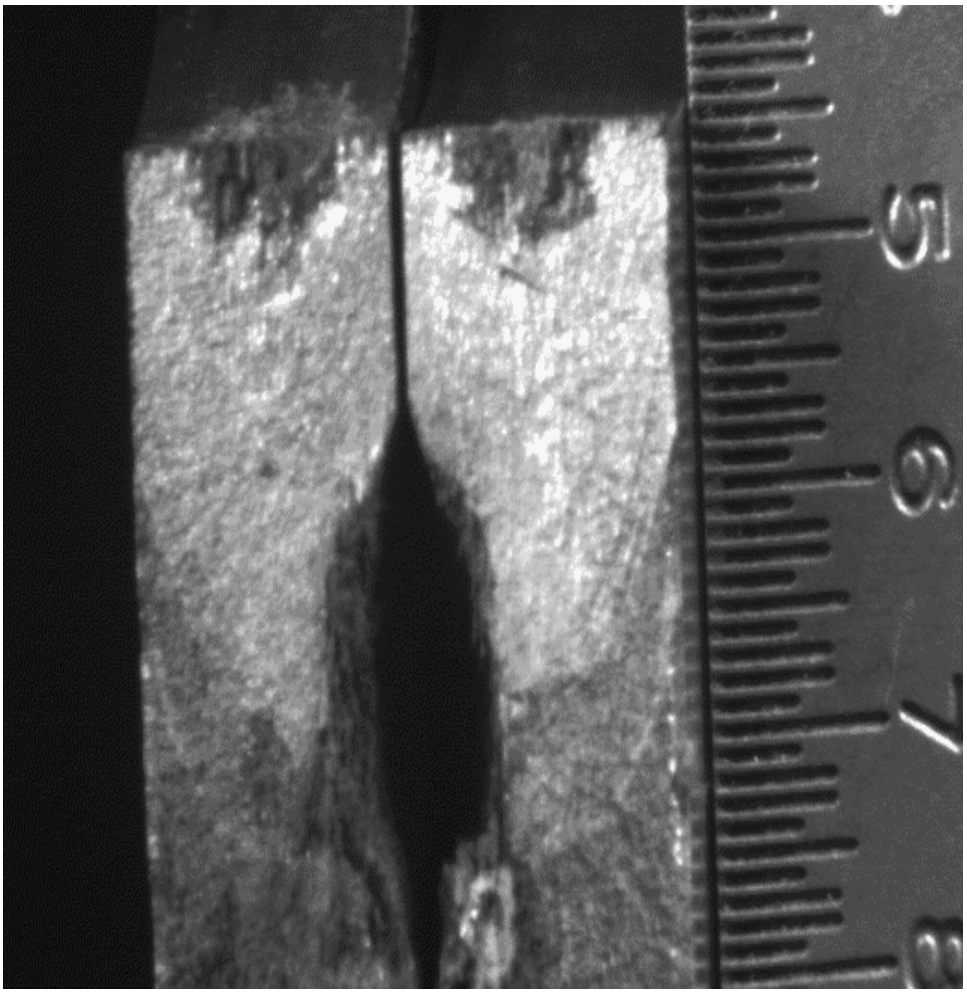

Figure 35. Fatigue cracking clearly nucleated at the side of the specimen where corrosion exists. Luster of the beach mark and radiating striations on both fracture surfaces are shown. Scale marks are in 1/100" increments.

Altogether, the specimens nucleated at IC locations or in the corners between corrosion on the "front" and "side" where these conditions existed collectively. The K_t of the pit (not the global specimen geometry) may have caused nucleation if the corrosion did not. These aspects are very difficult to determine with the number of variables here.

5. Discussion

At a glance, it seems as if the corroded faces of the specimens with transverse loading direction where both faces were corroded was the most damaging condition since all three of those replicates tested ended in failure. The faces that were exposed to the electrochemical procedure were the LT and ST planes. Failure is driven by the orientation of the exfoliation and the loading orientation. The data is inconclusive for the LT condition in the longitudinal loading direction and the ST condition in the transverse loading direction.

Corrosion should travel quickly along the longitudinal plane of the aluminum alloy, which could obviously have an effect on the load-carrying capability of the material. For example, a specimen with loading direction in the L (spanwise) direction with corrosion on the front would have more load carrying capability than the same corrosion condition on the specimens loaded in the T (chordwise) direction. This would be the case because the corrosion would travel across the net section, in the longitudinal direction, destroying load-carrying material. However, there were no specimens that failed in the suspected severe condition (T-direction loading with corrosion on LT plane) and only one of those specimens failed in the L-direction.

As another note on loss of net section, all but one of the specimens that were corroded on "both" faces failed. This is true for longitudinal loading and transverse. Again, this may be attributed to net section loss across the narrowest portion of the hourglass specimen.

From Table 5 and Table 6, the fatigue lives and depth of corrosion damage are listed. For nominally similar tests, the fatigue life scatter should be low. Using the widely used method proposed by Schijve [9], scatter is considered low when

$$\sigma_{\log(N_f)} \leq 0.15 \tag{2}$$

For the specimens that failed, $\sigma_{\log(Nf)} = 0.18$ which is acceptable considering the depth of damage and loading direction is different for many of the specimens tested.

The fatigue test frames had different cycling frequency because they were of differing capacities. Some large frames were used that could not cycle quickly due to their large size and therefore increased the time exposed to damaging humidity. Testing at slower frequencies would allow more time elapsed between each cycle; therefore the crack tip had more exposure to the damaging environment. However, there were no time-related correlations that were found between failed and un-failed specimens. Table 7 shows the number of cycles to failure and the frequency at which testing was done during both spectra.

Table 7. Comparative analysis of cycles to failure vs. test frequency

L	cycles to failure	test frame during spectrum	test frame during 1.2x spectrum
LT	6,015,498	55 kip MTS (7.8 Hz)	11 kip MTS (13.6 Hz)
LTLS	7,157,886	55 kip MTS (7.8 Hz)	11 kip MTS (13.6 Hz)
LTLS	2,740,914	11 kip MTS (13.6 Hz)	50 kip SATEC (2.4 Hz)
T	cycles to failure		
LTST	4,644,128	10 kip MTS (15.5 Hz)	10 kip MTS (15.5 Hz)
LTST	5,120,304	10 kip MTS (15.5 Hz)	20 kip SATEC (2.8 Hz)
LTST	9,192,452	10 kip MTS (15.5 Hz)	10 kip MTS (15.5 Hz)
ST	3,251,101	55 kip MTS (7.8 Hz)	11 kip MTS (13.6 Hz)

Also, it is important to note that none of the specimens failed during the first fatigue spectrum. This means that under severe environmental conditions, as simulated by the 100% relative humidity with the corrosive compound in the intergranular fissures, *the corroded upper wing skin is insensitive to fatigue in its first two lifetimes, 20,000 flight hours, at WS320*. Since the stresses are lower outboard of WS 320, the conclusion can be drawn that *exfoliation damage from WS320 and outboard is fatigue insensitive*. Specimens were first tested using a spectrum with a maximum stress of 16.8 ksi. In the second round of testing, a stress level of 20.16 ksi was used to expose the specimens to a more severe loading condition. This stress level proved fatal for seven of the fifteen successful tests.

AFGROW, developed by the Air Force Research Laboratory, is a widely used program in the Department of Defense to perform crack growth analysis and life prediction. This program is very useful in validating new structures and predicting the life of aging platforms. In AFGROW, a specimen with a corrosion site on the side was input to model the actual dimensions of the test pieces. Material data used was AA 7178-T6. The spectrum used for testing was the same as that used in AFGROW analysis. Detailed inputs for AFGROW are given in Appendix C. The program showed a quite substantial decrease in number of cycles to failure as the maximum stress was multiplied by 1.2. The unaltered spectrum was capable of running 355,372 cycles before failure while the spectrum at 20.16 ksi ran for only 155,967 cycles. Thus, a 20% increase in applied stress results in a more than 50% reduction in fatigue life. The predicted life is all crack growth whereas the actual fatigue life is composed of crack nucleation time and crack growth. Figure 36 shows a screen shot of the crack growth data produced in AFGROW using the specimens discussed here as the model.

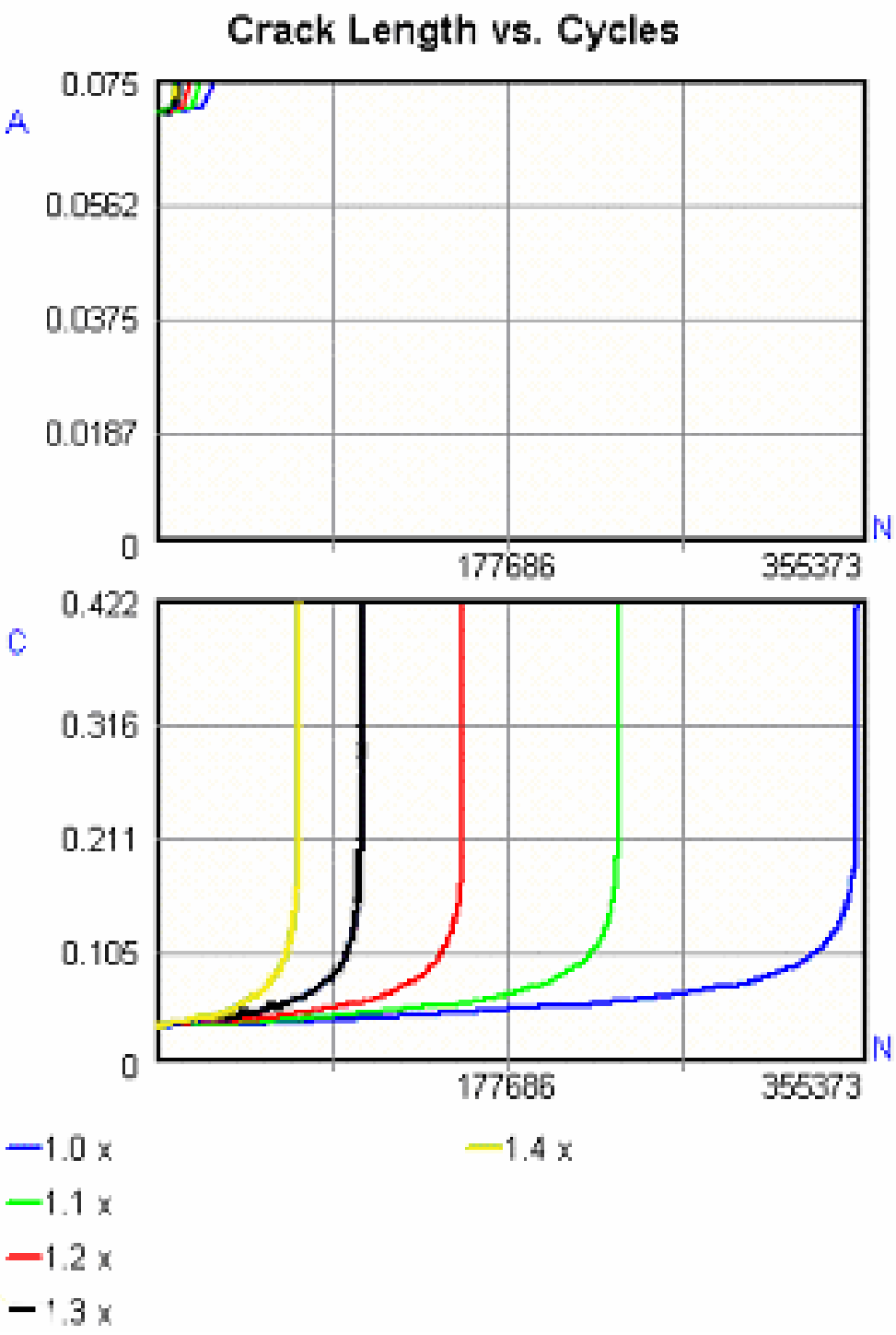

Figure 36. Crack length vs. number of cycles to failure for specimen selected to run a simulated crack growth test

The significance of the AFGROW result is that a 1.2 multiplier on the tension peaks has a severe limiting factor on the fatigue life of the specimens. Using the more severe spectrum, the specimen would ideally last about half as long as the unaltered condition.

6. Conclusion and Recommendations

Multiple material orientations (LT, ST, LS) and loading directions (LT and TL) in the aluminum alloy 7178-T6 were fatigue tested to two lifetimes, 20,000 cycles. All 15 specimens survived two lifetimes. To nucleate failure, the tensile peaks of the E-8C UWS spectrum were increased by 20%. Seven specimens failed at the higher stress level. Several observations and conclusions can be drawn from this experimental investigation.

- The hourglass specimen design was not optimal for this investigation as the test section was too small.
  - A new specimen design has been used in the follow-on investigation.
- The corrosion protocol used did not corrode the specimens to the desired depth of 30% of the specimen thickness on the LS and ST planes. The corrosion protocol did work in a sense on the LT plane where the desired depth was obtained; however, this surface was machined prior to corroding. In other words, the depth on the LT plane was obtained by a combination of machining and corroding.
- The location of the crack nucleation site varied.
  - 2 nucleated at corrosion damage.
    - Beach marks had formed circumferentially around the corrosion site where the center of the radius is at the corrosion.
  - 2 nucleated where there was no visible corrosion damage detectable.
    - One specimen seemed to have experienced shear loading and failed due to that. Another had no indication of corrosion damage nucleation at the fault site.
  - 3 nucleated at locations between corrosion.
    - These failures occurred between the corrosion on the front and the corrosion on the side. The likely cause for failure was the weakness of the surviving material between corroded areas.
- A subtle dependence on loading direction was observed as more specimens failed when loaded in the TL direction. This result is not surprising as the crack growth rates are higher in the TL than LT direction for this alloy.
- Although the tests were conducted in an aggressive environment, no frequency dependence was seen in the range of 2.4 – 15.5 Hz.
- The scatter in the fatigue lives was acceptable with a $\sigma_{\log(Nf)} = 0.18$
- Fatigue life predictions do not correlate well to the actual fatigue lives because the predicted lives do not account for crack nucleation time which makes up a large portion of the fatigue life.
- Intergranular corrosion and exfoliation corrosion damage in the E-8C UWS is fatigue insensitive.
  - From a fatigue point of view, intergranular and exfoliation corrosion does not need to be removed when extent of corrosion is within the TO limits of 30% thickness loss.

7. Reference

1. Dowling, Norman E. Mechanical Behavior of Materials: Engineering Methods for Deformation, Fracture, and Fatigue. p 296 Second Edition. Prentice-Hall © 1999
2. Niu, Michael C.Y. Airframe Structural Design p 115 Conmilit Press Ltd. © 1988
3. Frankel, Gerald S. and Rokhlin, Stanislav I. "Intergranular and Exfoliation Corrosion Rate Studies" The Ohio State University, 23 February 2003.
4. Email correspondence between Fawaz and Frankel 11 May 2004
5. MIL HDBK 1530B General Guidelines for Aging Aircraft Structural Integrity Program, Department of Defense Handbook 3 July 2002
6. Beer and Johnston, Mechanics of Materials, p 531 McGraw-Hill New York, ©1981.
7. MIL HDBK 5J Metallic Materials and Elements for Aerospace Vehicle Structures, Department of Defense Handbook 31 January 2003
8. "Preliminary Study into the Effect of Exfoliation Corrosion on Aircraft Structural Life Extension" Bellinger, N.C., Komorowski, J.P., Liao M., Carmody D., Foland T., and Peeler, D. 6th Joint FAA/DoD/NASA Aging Aircraft Conference— 16-19Sept. 2002
9. Schijve, J. "Fatigue Predictions and Scatter." Fatigue and Fracture of Engineering Materials and Structures. 17 (1994): 381-396.

Appendix A. Description of Specimen

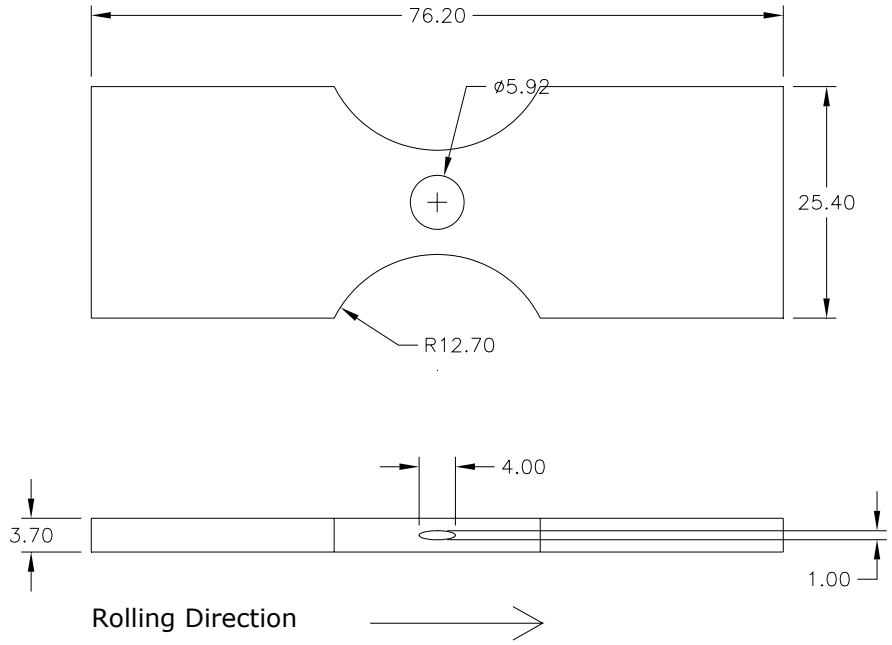

Figure A1. Specimen dimensions with corrosion on LT and LS planes

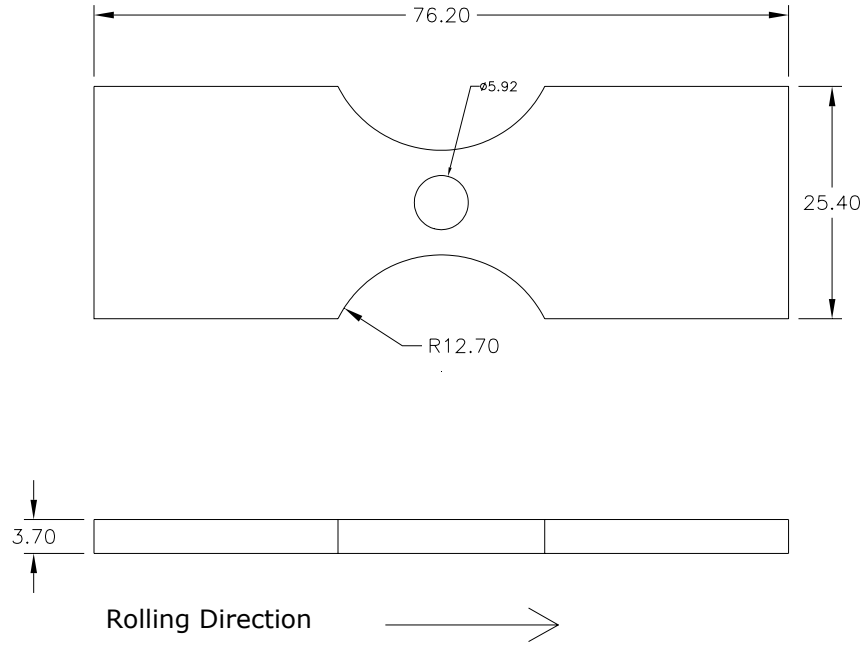

Figure A2. Specimen dimensions with corrosion on LT plane

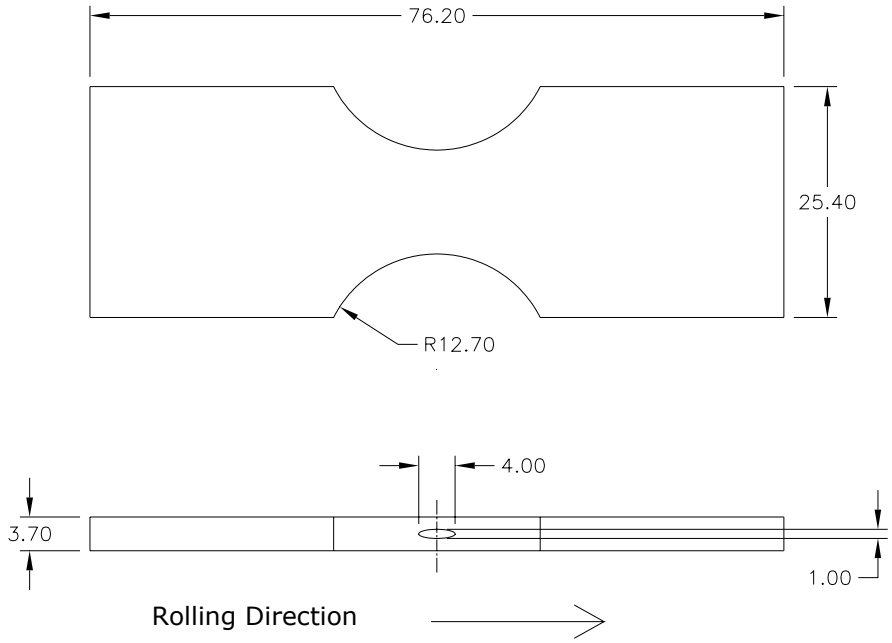

Figure A3. Specimen dimensions with corrosion on LS plane

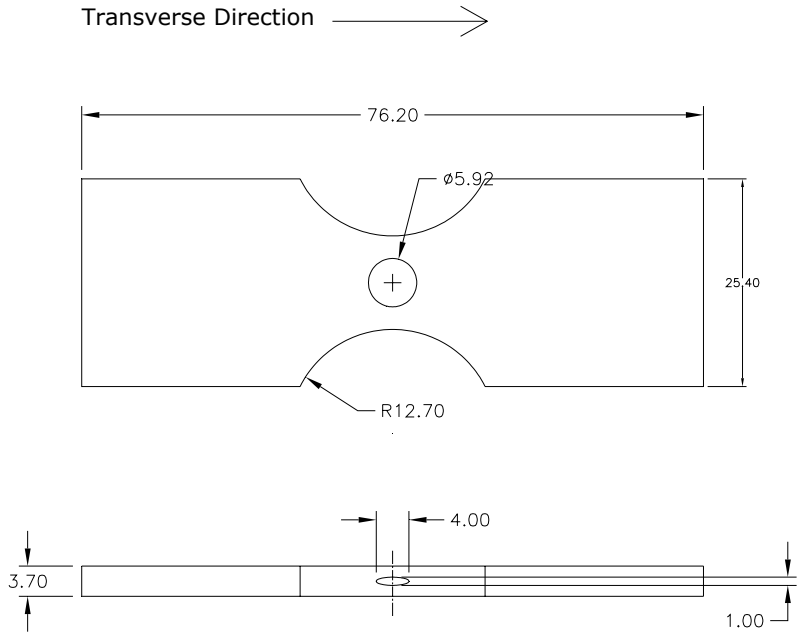

Figure A4. Specimen dimensions with corrosion on LT and ST planes

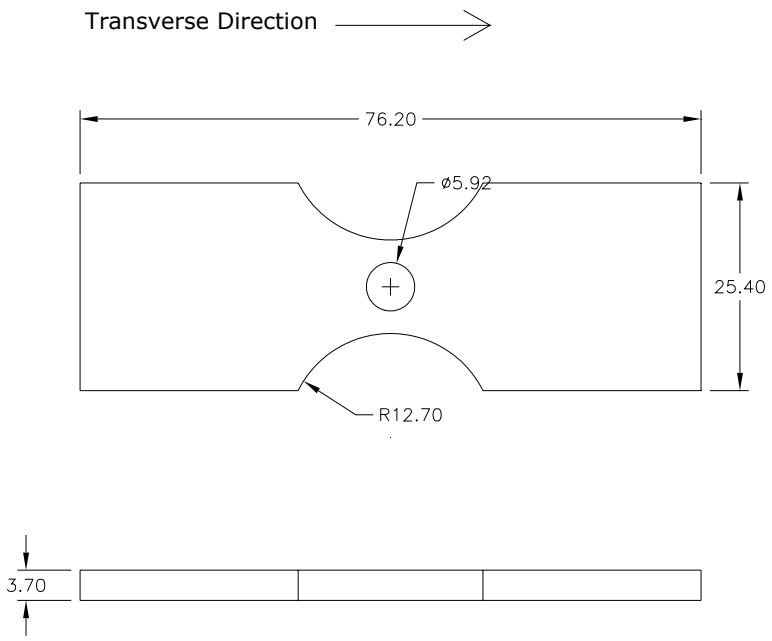

Figure A5. Specimen dimensions with corrosion on LT plane.

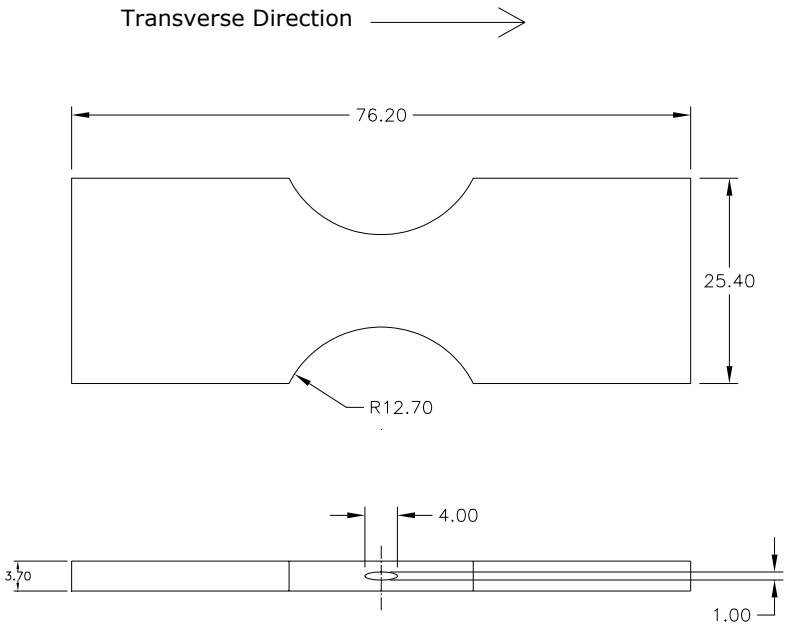

Figure A6. Specimen dimensions with corrosion on ST plane.

Appendix B. Images from Serial Sectioning Showing Loss in Cross-Sectional Area

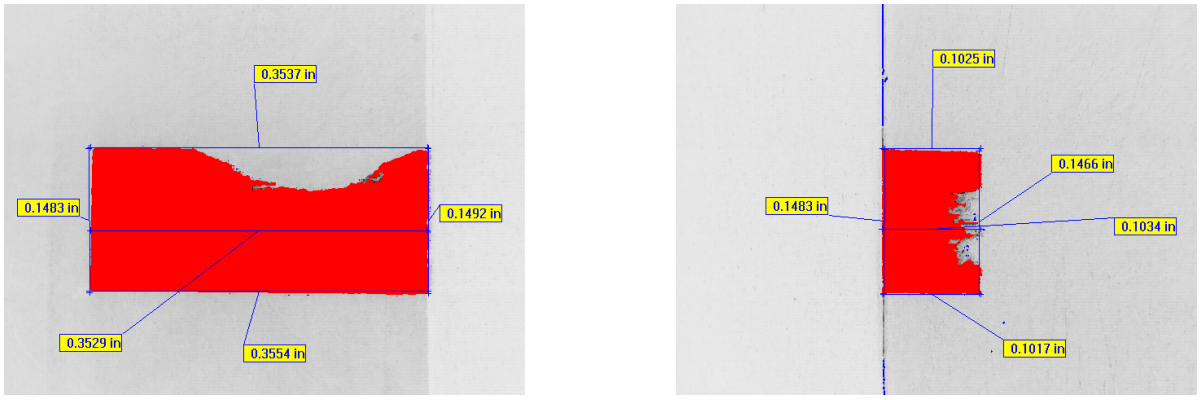

Figure B1. Specimen loaded in L direction with corrosion on LT and LS planes, replicate number one.

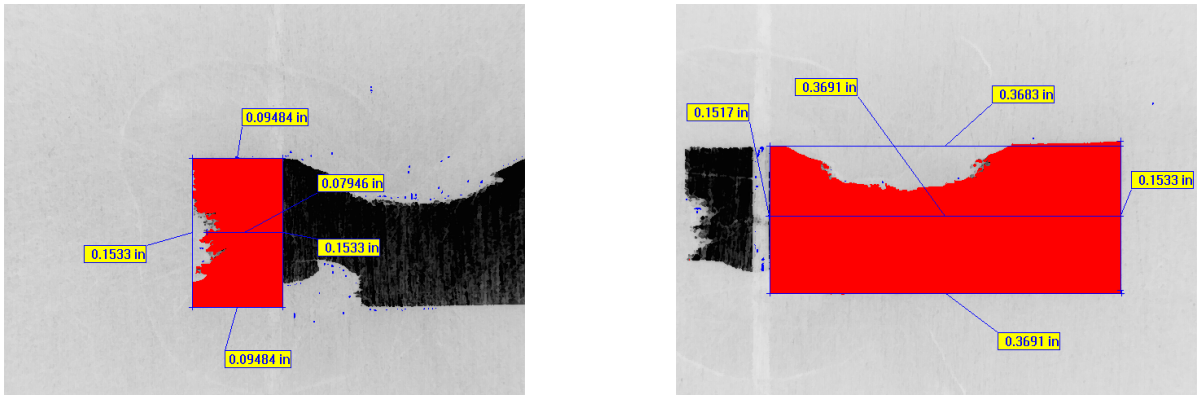

Figure B2. Specimen loaded in L direction with corrosion on LT and LS planes, replicate number three.

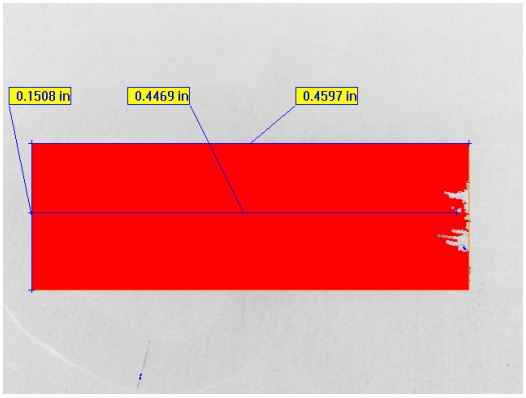

Figure B3. Specimen loaded in L direction with corrosion on LS plane, replicate number one.

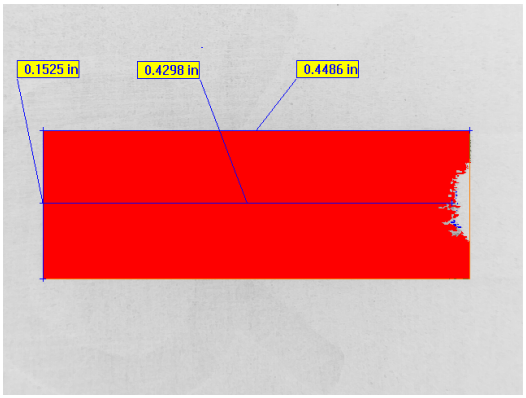

Figure B4. Specimen loaded in L direction with corrosion on LS plane, replicate number two.

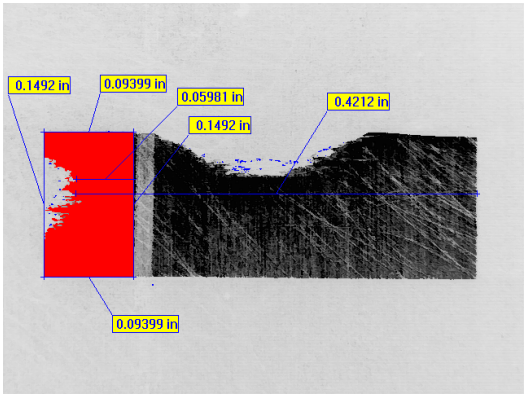

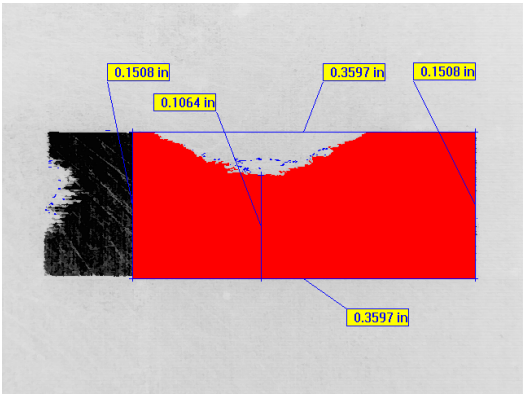

Figure B5. Specimen loaded in T direction with corrosion on LT and ST planes, replicate number one.

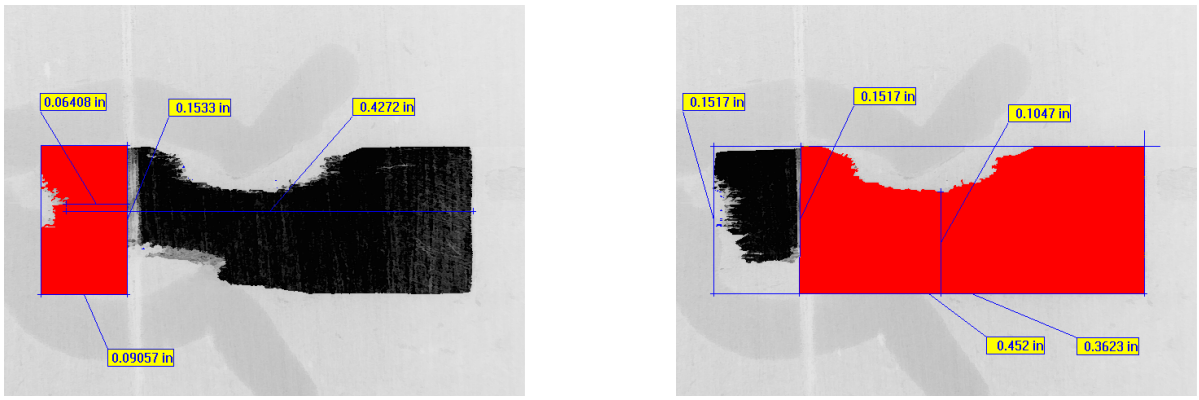

Figure B6. Specimen loaded in T direction with corrosion on LT and ST planes, replicate number two.

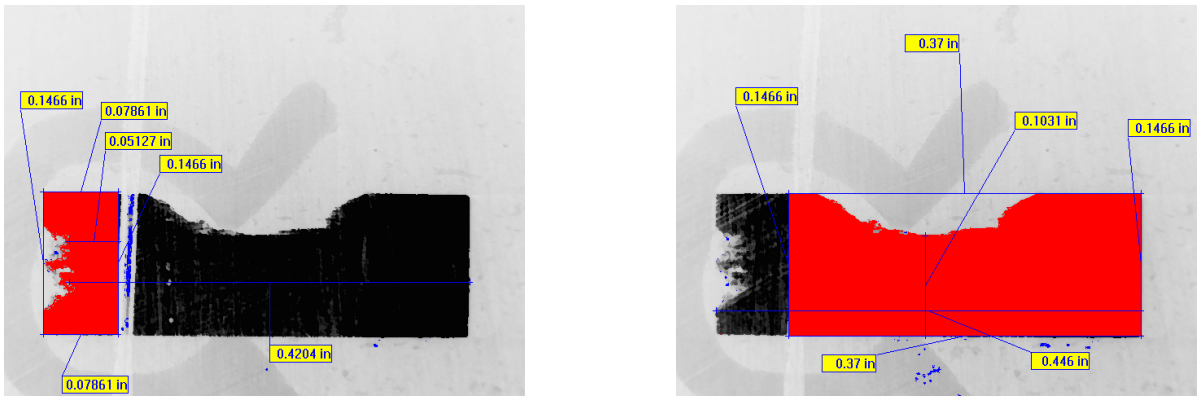

Figure B7. Specimen loaded in T direction with corrosion on LT and ST planes, replicate number three.

Appendix C. AFGROW Input Data

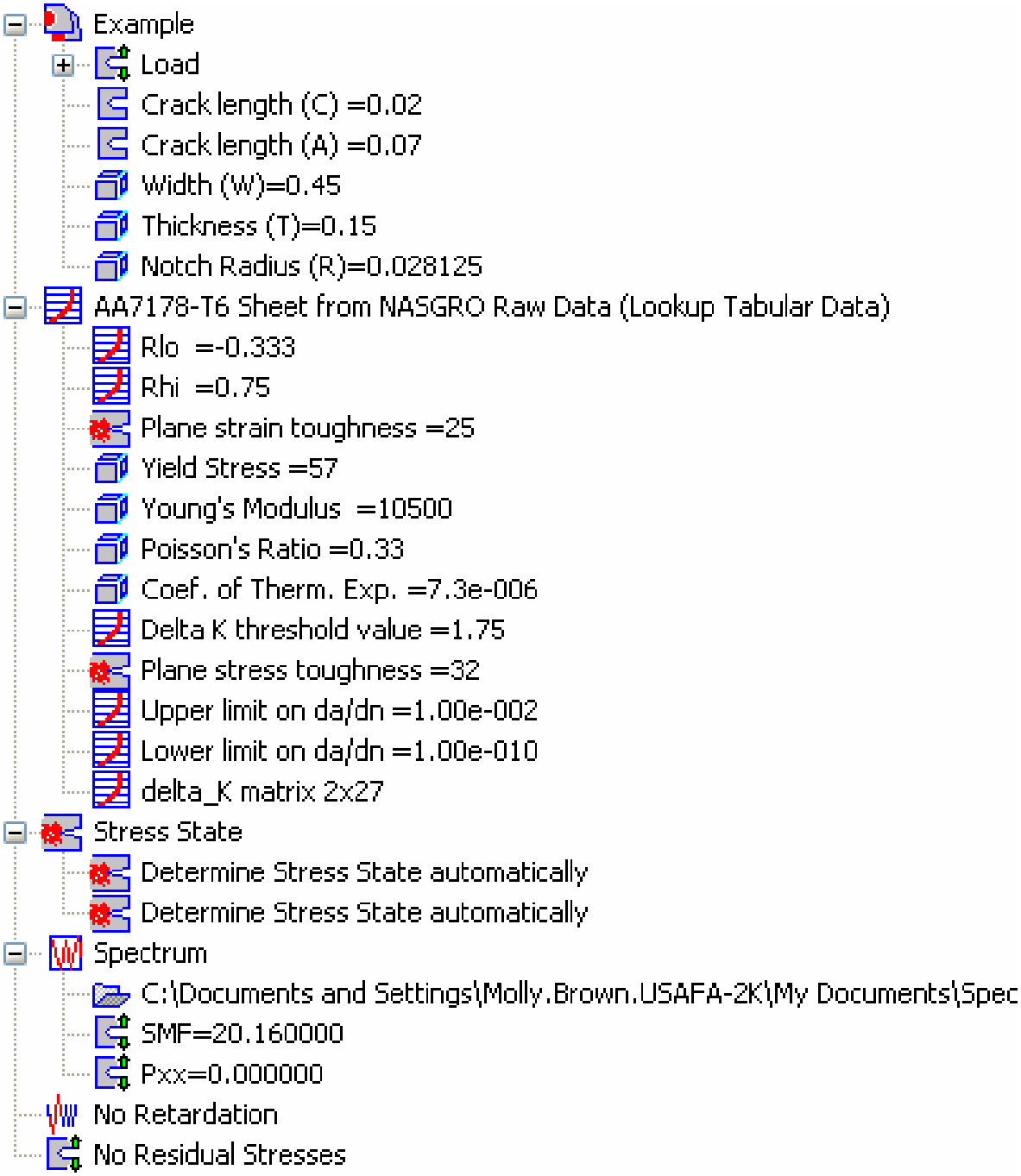

Figure C1. Screen shot of AFGROW input parameters used in the present work.

Table C1. Tabular data used for AA 7178 material input file in the present work.

da/dN (in/cycle)	ΔK (ksi $\sqrt{in}$) for R=0	ΔK (ksi $\sqrt{in}$) for R=0.5
3.94E-09	1.593	0.919
3.94E-08	1.597	0.921
7.87E-08	1.602	0.924
3.94E-07	1.684	0.951
7.87E-07	1.82	0.992
1.57E-06	2.275	1.229
2.36E-06	2.821	1.547
3.94E-06	3.272	1.934
7.87E-06	3.822	2.489
1.18E-05	4.232	2.774
1.57E-05	4.55	2.945
2.36E-05	4.887	3.155
3.94E-05	5.324	3.365

da/dN (in/cycle)	ΔK (ksi $\sqrt{in}$) for R=0	for R=0.5
7.87E-05	5.87	3.777
0.000157	6.63	4.323
0.000236	7.371	4.687
0.000394	9.055	5.46
0.000787	11.376	6.951
0.001575	14.561	8.611
0.003937	19.111	10.891
0.007874	22.751	12.447
0.015748	26.755	13.997
0.023622	29.577	15.016
0.031496	31.397	15.744
0.03937	32.534	16.29
0.15748	37.312	18.747
0.393701	38.222	19.248

Ultimate Strength	66	ksi
Coefficient of Thermal Expansion	7.3 E-6	/°F
da/dN hi	0.01	in/cycle
plane stress fracture toughness	32	ksi $\sqrt{in}$
plane strain fracture toughness	25	ksi $\sqrt{in}$
delta K threshold at R=0	1.75	ksi $\sqrt{in}$
Young's Modulus	10500	ksi
Poisson's Ratio	0.33	
da/dN lo	1.00E-10	in/cycle
yield strength	57	ksi
lower limit on R shift	-0.333	
upper limit on R shift	0.75	